

# Effects of neutrino oscillations on nucleosynthesis and neutrino signals for an $18M_{\odot}$ supernova model

Meng-Ru Wu,<sup>1,2</sup> Yong-Zhong Qian,<sup>2</sup> Gabriel Martínez-Pinedo,<sup>1,3</sup> Tobias Fischer,<sup>4</sup> and Lutz Huther<sup>1</sup>

<sup>1</sup>*Institut für Kernphysik (Theoriezentrum), Technische Universität Darmstadt, Schlossgartenstraße 2, 64289 Darmstadt, Germany*

<sup>2</sup>*School of Physics and Astronomy, University of Minnesota, Minneapolis, Minnesota 55455, USA*

<sup>3</sup>*GSI Helmholtzzentrum für Schwerionenforschung, Planckstraße 1, 64291 Darmstadt, Germany*

<sup>4</sup>*Institute for Theoretical Physics, University of Wrocław, Pl. M. Borna 9, 50-204 Wrocław, Poland*

(Received 30 December 2014; published 13 March 2015)

In this paper, we explore the effects of neutrino flavor oscillations on supernova nucleosynthesis and on the neutrino signals. Our study is based on detailed information about the neutrino spectra and their time evolution from a spherically symmetric supernova model for an  $18M_{\odot}$  progenitor. We find that collective neutrino oscillations are not only sensitive to the detailed neutrino energy and angular distributions at emission, but also to the time evolution of both the neutrino spectra and the electron density profile. We apply the results of neutrino oscillations to study the impact on supernova nucleosynthesis and on the neutrino signals from a Galactic supernova. We show that in our supernova model, collective neutrino oscillations enhance the production of rare isotopes  $^{138}\text{La}$  and  $^{180}\text{Ta}$  but have little impact on the  $\nu p$ -process nucleosynthesis. In addition, the adiabatic Mikheyev-Smirnov-Wolfenstein flavor transformation, which occurs in the C/O and He shells of the supernova, may affect the production of light nuclei such as  $^7\text{Li}$  and  $^{11}\text{B}$ . For the neutrino signals, we calculate the rate of neutrino events in the Super-Kamiokande detector and in a hypothetical liquid argon detector. Our results suggest the possibility of using the time profiles of the events in both detectors, along with the spectral information of the detected neutrinos, to infer the neutrino mass hierarchy.

DOI: [10.1103/PhysRevD.91.065016](https://doi.org/10.1103/PhysRevD.91.065016)

PACS numbers: 14.60.Pq, 26.30.-k, 97.60.Bw

## I. INTRODUCTION

Core-collapse supernovae signify the death of massive stars heavier than  $\sim 8M_{\odot}$  and the birth of proto-neutron stars. In each explosion,  $\sim 10^{53}$  erg of gravitational binding energy is released through emission of  $\sim 10^{58}$  neutrinos (antineutrinos) of all three flavors over  $\sim 10$  s. These neutrinos play essential roles in the dynamics and nucleosynthesis of supernovae. Prominent examples include revival of the stalled supernova shock by neutrino heating in conjunction with fluid instabilities ([1]; see [2] for a review), production of heavy elements in neutrino-driven winds from proto-neutron stars (e.g., [3]; see [4] for a recent review), and neutrino-induced nucleosynthesis in outer shells of supernovae (e.g., [5–8]). In addition, current and planned 10-kiloton-scale detectors are able to observe thousands of neutrino events if a supernova occurs in the Galaxy (see [9] for a review). Such detection would provide a unique opportunity to explore the physics of core-collapse supernovae and properties of neutrinos.

In the absence of flavor oscillations, we would only need the emission characteristics of neutrinos determined by their decoupling from the proto-neutron star, such as their luminosities, energy spectra, and angular distributions, in order to understand their roles in supernovae. It would also be straightforward to infer the neutrino luminosities and energy spectra at emission from signals in appropriate detectors for a

Galactic supernova. However, neutrino oscillations have been established by various experiments. Consequently, we must take neutrino flavor evolution into account when assessing the effects of neutrinos on the dynamics and nucleosynthesis of supernovae and when deciphering the rich underlying physics from supernova neutrino signals. In this paper we present a framework for calculating neutrino flavor evolution in the dynamic supernova environment, perform detailed calculations for an  $18M_{\odot}$  supernova model, and examine the effects of neutrino oscillations on nucleosynthesis and neutrino signals for this model.

The intrinsic parameters describing neutrino oscillations include three vacuum mixing angles ( $\theta_{12}$ ,  $\theta_{13}$ ,  $\theta_{23}$ ), a  $CP$ -violating phase ( $\delta_{CP}$ ), and two independent mass-squared differences (e.g.,  $\Delta m_{21}^2 \equiv m_2^2 - m_1^2$ ,  $\Delta m_{31}^2 \equiv m_3^2 - m_1^2$ ) between neutrino vacuum mass eigenstates. Observations of solar and atmospheric neutrinos and other terrestrial experiments have measured  $\theta_{12}$ ,  $\theta_{13}$ ,  $\theta_{23}$ ,  $\Delta m_{21}^2$ , and  $|\Delta m_{31}^2|$  to good precision (see review in [10]). There are ongoing and planned experiments to measure the yet unknown  $\delta_{CP}$  and sign of  $\Delta m_{31}^2$ . The latter is also referred to as the neutrino mass hierarchy, with  $\Delta m_{31}^2 > 0 (< 0)$  defined as normal (inverted). In this paper we assume  $\delta_{CP} = 0$  but consider both normal and inverted mass hierarchies.

We divide the supernova environment into two regions separated by a “decoupling sphere” at radius  $r = R_d$ .

We assume that at  $r < R_d$ , neutrino interactions with matter dominate and flavor oscillations have no net effect. Classical Boltzmann transport equations coupled with supernova conditions then determine the energy and angular distributions  $f_\nu(t_{\text{em}}, E, \theta, R_d)$  for neutrinos emitted at  $r = R_d$ , where  $t_{\text{em}}$  is the time of emission,  $E$  is the neutrino energy, and  $\theta_d$  is the angle of propagation with respect to the radial direction at  $r = R_d$  (see Fig. 1). An important feature of these distributions is the hierarchy of the corresponding average neutrino energies  $\langle E_{\nu_e} \rangle < \langle E_{\bar{\nu}_e} \rangle < \langle E_{\nu_\mu(\tau)} \rangle \approx \langle E_{\bar{\nu}_\mu(\tau)} \rangle$ . At  $r > R_d$ , only a small fraction of neutrinos can still interact with matter to affect supernova dynamics and nucleosynthesis. For the purpose of treating neutrino flavor evolution, we assume that all neutrinos are free-streaming at  $r > R_d$ .

Flavor evolution of neutrinos at  $r > R_d$  can exhibit rich phenomena because they propagate through an enormous range of matter density, the structure of which may be complicated by convection-driven fluctuations and propagation of the supernova shock. These factors influence neutrino oscillations through the Mikheyev-Smirnov-Wolfenstein (MSW) effect induced by forward scattering of neutrinos on electrons [11,12]. In addition, due to the nonlinear coupling through forward scattering of neutrinos on other neutrinos, collective oscillations among all three flavors of neutrinos (antineutrinos) may occur within  $\sim 100$  km of the proto-neutron star (see [13] for a review and [14–36] for more recent developments). In any case, as  $\nu_\mu$ ,  $\bar{\nu}_\mu$ ,  $\nu_\tau$ , and  $\bar{\nu}_\tau$  have higher average energies than  $\nu_e$  and  $\bar{\nu}_e$  at emission, flavor oscillations at  $r > R_d$  may have important effects on supernova dynamics, nucleosynthesis, and neutrino signals.

While neutrino oscillations in supernovae have been studied extensively, our approach in this paper differs from these previous works in that we employ neutrino emission characteristics and electron number density profiles calculated self-consistently by a supernova model and that we explicitly take the time evolution of these quantities into account when calculating neutrino flavor evolution through the supernova environment over the period of significant neutrino emission. The following example illustrates why such an approach is required to adequately examine the impact of neutrino oscillations on supernova physics. Consider a mass element moving along a radial trajectory

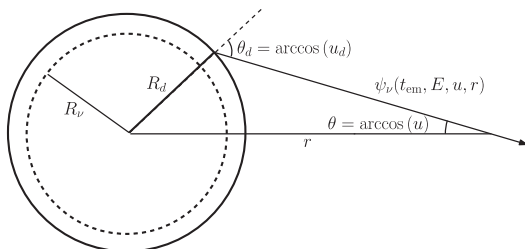


FIG. 1. Sketch of neutrino emission and propagation.

$r_m(t)$ , and for simplicity, ignore the neutrino travel time from emission to reaching the mass element. To calculate the rates of neutrino reactions in this mass element, we need quantities such as  $P_{\nu_e \nu_e}(t_{\text{em}}, E, \theta, r)$  for  $t_{\text{em}} = t$  and  $r = r_m(t)$ , which gives the survival probability for a  $\nu_e$  emitted with energy  $E$  at time  $t_{\text{em}}$  and arriving at radius  $r > R_d$  with an angle of propagation  $\theta$  with respect to the radial direction (see Fig. 1). As the process of nucleosynthesis in the mass element can last up to  $\sim 10$  s and there are large changes in  $r_m$ , neutrino emission characteristics, and the electron number density profile over this time, we must calculate  $P_{\nu_e \nu_e}(t_{\text{em}}, E, \theta, r)$  and similar survival probabilities for many time snapshots of the supernova input for neutrino flavor evolution. Therefore, our results on neutrino oscillations are given in terms of these survival probabilities on an extensive four-dimensional grid covering wide ranges of emission time, neutrino energy, propagation angle, and arrival radius. Our methodology is demonstrated for a specific  $18M_\odot$  supernova model and can be generalized to any spherically symmetric models.

We find that collective oscillations are sensitive to the details of the neutrino energy and angular distributions at emission and to the time evolution of these distributions and the electron number density profile. For the specific model studied, although collective neutrino oscillations occur too far out to affect nucleosynthesis in the neutrino-driven wind, they can still affect neutrino-induced nucleosynthesis in outer supernova shells in combination with the MSW effect. We show that for a Galactic supernova described by the same model, the neutrino signals are mainly modified by the MSW effect and those signals during shock revival can be used to infer the yet unknown neutrino mass hierarchy.

We describe the supernova model in Sec. II and our approach to calculate neutrino flavor evolution in Sec. III. We present and discuss our results on neutrino oscillations in Sec. IV. We apply these results to assess the effects of neutrino oscillations on nucleosynthesis in Sec. V and to analyze the neutrino signals in Super-Kamiokande and a hypothetical liquid argon detector in Sec. VI. We discuss all our results and conclude in Sec. VII.

## II. SUPERNOVA MODEL

We adopt a supernova model with an  $18M_\odot$  progenitor. This model is based on general-relativistic radiation hydrodynamics in spherical symmetry and incorporates detailed three-flavor Boltzmann neutrino transport [37]. The core collapse is initiated by loss of energy and pressure through photo-disintegration of iron-group nuclei and capture of electrons on protons and nuclei. Neutrinos produced during the collapse are predominantly  $\nu_e$ , which are trapped and can only diffuse out of the core with  $\langle E_{\nu_e} \rangle \approx 4\text{--}9$  MeV [see Fig. 2(d)]. A shock is launched when the inner core bounces upon reaching supra-nuclear density. As the shock

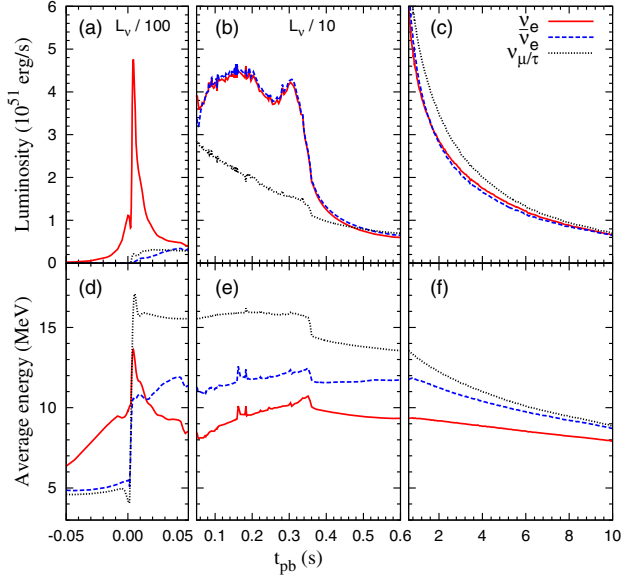


FIG. 2 (color online). Evolution of neutrino luminosities [panels (a)–(c)] and average energies [panels (d)–(f)] for the  $18M_{\odot}$  supernova model as observed at infinity [37].

passes through the neutrino trapping surface, i.e., the “neutrinosphere” at a density of  $\rho \sim 10^{12}$  g/cm<sup>3</sup>, protons liberated from nuclei by shock heating rapidly capture electrons to produce a burst of  $\nu_e$  on a timescale of  $\sim 10$  ms [see Fig. 2(a)]. The luminosity of this so-called neutronization  $\nu_e$  burst is  $\sim 10^{53}$  erg/s and can provide a potential diagnostic of the neutrino mass hierarchy [38] (see Sec. VI for further discussion). The subsequent neutrino emission has comparable luminosities for neutrinos and antineutrinos of all three flavors (see Fig. 2). The timescale of  $\sim 10$  s for this emission is determined by neutrino diffusion out of the newly formed proto-neutron star.

The shock launched by core bounce is not energetic enough to break out of the outer core. It is stalled at  $r_{\text{sh}} \sim 100$  km and becomes an accretion shock through which matter can fall onto the proto-neutron star. During this accretion phase, the luminosities of  $\nu_e$  and  $\bar{\nu}_e$  are nearly twice as high as those of  $\nu_{\mu(\tau)}$  and  $\bar{\nu}_{\mu(\tau)}$  [see Fig. 2(b)]. This is because emission of  $\nu_e$  and  $\bar{\nu}_e$  is enhanced by efficient charged-current reactions (dominantly  $e^{\pm}$  capture on free nucleons) in the extended region above the proto-neutron star while that of  $\nu_{\mu(\tau)}$  and  $\bar{\nu}_{\mu(\tau)}$  is dominated by diffusion out of the proto-neutron star. Absorption of some  $\nu_e$  and  $\bar{\nu}_e$  can heat the material at  $r < r_{\text{sh}}$ , thereby reviving the stalled shock [1]. However, recent studies suggest that this so-called neutrino-driven explosion mechanism works robustly only for low-mass progenitors but must be combined with convection to deliver explosion for higher-mass progenitors (see [2] for a review). In the latter case, multidimensional simulations are required.

As an approximation to the effects of convection in multidimensional supernova models, neutrino heating in

the region between the neutrinosphere and the stalled shock is artificially enhanced in our spherically symmetric model to trigger the explosion, thereby allowing us to study the long-term evolution of the proto-neutron star up to a time post (core) bounce of  $t_{\text{pb}} \sim 10$  s. Once the shock is revived at  $t_{\text{pb}} \sim 350$  ms, accretion of matter by the proto-neutron star quickly diminishes, resulting in a sharp drop of  $\nu_e$  and  $\bar{\nu}_e$  luminosities [see Fig. 2(b)]. In the subsequent proto-neutron star cooling phase, the luminosities of  $\nu_{\mu(\tau)}$  and  $\bar{\nu}_{\mu(\tau)}$  become slightly higher than those of  $\nu_e$  and  $\bar{\nu}_e$ , because the former decouple from regions of higher temperature as reflected by their average energy [see Fig. 2(f)]. In general, the canonical average energy hierarchy of  $\langle E_{\nu_e} \rangle < \langle E_{\bar{\nu}_e} \rangle < \langle E_{\nu_{\mu(\tau)}} \rangle \approx \langle E_{\bar{\nu}_{\mu(\tau)}} \rangle$  holds throughout the accretion and cooling phases in our model [see Figs. 2(e) and 2(f)].

During the cooling phase,  $\nu_e$  and  $\bar{\nu}_e$  continue to heat the material immediately outside the proto-neutron star, giving rise to a matter outflow usually referred to as the neutrino-driven wind. Specifically, free neutrons and protons in the wind material at high density and temperature can absorb  $\nu_e$  and  $\bar{\nu}_e$ , respectively, through

$$\nu_e + n \rightarrow p + e^-, \quad (1a)$$

$$\bar{\nu}_e + p \rightarrow n + e^+. \quad (1b)$$

This neutrino heating drives the wind to expand rapidly on timescales of  $\sim 10$  ms (see Fig. 3). Under such conditions elements heavier than iron can form when the wind expands to low density and temperature. A key parameter governing this nucleosynthesis is the electron fraction  $Y_e$ , which is determined by the competition between reactions (1a) and (1b). If  $\nu_e$  and  $\bar{\nu}_e$  had the same luminosities and energy spectra, reaction (1a) would proceed faster than reaction (1b) because the former is favored by the neutron-proton mass difference  $\Delta$  [see Eq. (17)]. In order to obtain a neutron-rich wind with  $Y_e < 0.5$  required for the rapid neutron-capture process (e.g., [4]), the average energy of  $\bar{\nu}_e$  must exceed that of  $\nu_e$  by approximately  $4\Delta$  with the same luminosity for  $\bar{\nu}_e$  and  $\nu_e$  [3]. While the luminosities are approximately the same, the average energy for  $\bar{\nu}_e$  never exceeds that for  $\nu_e$  by  $4\Delta$  throughout the cooling phase in our model. Consequently, the wind is proton rich as shown in Fig. 3(d) for four selected mass elements. In this case, a  $\nu p$  process can occur [39–41].

The selected wind mass elements shown in Fig. 3 enclose baryonic masses of 1.58246, 1.58196, 1.58162, and 1.58131 in units of  $M_{\odot}$ , and are ejected from the proto-neutron star at  $t_{\text{pb}} = 0.840, 1.253, 1.726,$  and  $2.526$  s, respectively. The final abundances of nuclei produced by the  $\nu p$  process in these mass elements not only depend on their asymptotic  $Y_e$  but also on the rate of reaction (1b) when their temperature evolves through the range of  $1 \lesssim T \lesssim 3$  GK [39,40]. As shown in Fig. 3(b), these mass

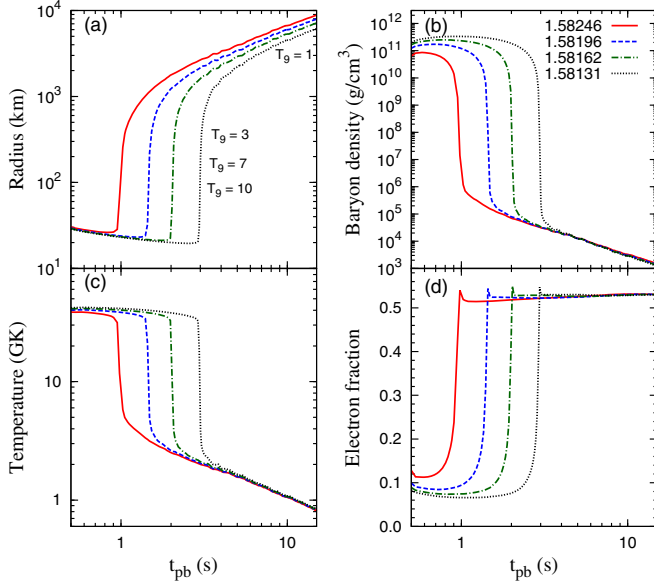


FIG. 3 (color online). Evolution of (a) radius, (b) density, (c) temperature, and (d) electron fraction for four mass elements in the neutrino-driven wind of the  $18M_{\odot}$  supernova model. The mass elements are labeled by their enclosed baryonic masses in units of  $M_{\odot}$ . The radius and density at which the temperature in units of GK reaches  $T_9 = 10, 7, 3$ , and  $1$  are marked in panels (a) and (b).

elements stay in this temperature range for  $\sim 10$  s. During this time, the neutrino luminosities change by an order of magnitude, and so does the difference in average energy between  $\bar{\nu}_e$  and  $\bar{\nu}_{\mu(\tau)}$  (see Fig. 2). We will show that neutrino oscillations occur before the mass elements enter the above temperature range and the results are extremely sensitive to the evolution of neutrino energy spectra. Therefore, we must conduct a comprehensive study of neutrino oscillations for the entire cooling phase in order to examine their effects on nucleosynthesis in the neutrino-driven wind.

### III. METHODOLOGY OF CALCULATING NEUTRINO FLAVOR EVOLUTION

We adopt the following neutrino mixing parameters:  $\Delta m_{21}^2 = 7.59 \times 10^{-5} \text{ eV}^2$ ,  $|\Delta m_{31}^2| = 2.43 \times 10^{-3} \text{ eV}^2$ , and  $\sin^2 2\theta_{12} = 0.87$  [42]. Recent measurement of  $\bar{\nu}_e$  disappearance at Daya Bay gave  $\sin^2 2\theta_{13} = 0.092 \pm 0.016 \pm 0.005$  [43], which corresponds to a central value of  $\theta_{13} = 0.15$ . This is somewhat larger than the value of  $\theta_{13} = 0.1$  assumed in [44], a major study on collective oscillations. We perform a full set of calculations using  $\theta_{13} = 0.1$  for comparison with this previous study, but also carry out additional calculations using  $\theta_{13} = 0.15$ . We find that the results for these two values of  $\theta_{13}$  agree within 5% (see Sec. IV C). We consider both cases of  $\Delta m_{31}^2 > 0$  (normal mass hierarchy) and  $\Delta m_{31}^2 < 0$  (inverted mass hierarchy).

For easy separation of the normal and inverted mass hierarchies, we use a rotated flavor basis  $(|\nu_e\rangle, |\nu_x\rangle, |\nu_y\rangle)^T = R_{23}^{-1}(\theta_{23})(|\nu_e\rangle, |\nu_{\mu}\rangle, |\nu_{\tau}\rangle)^T$ , where  $R_{23}$  is the rotation matrix in the 2–3 subspace [45]. For all calculations we assume  $\delta_{CP} = 0$  (see [46] for discussion of generally small effects of  $\delta_{CP}$  on supernova neutrino oscillations).

Studies of neutrino oscillations outside the proto-neutron star are usually carried out by adopting a neutrino emission model similar to the “bulb model” in [44], where all neutrinos are assumed to be free-streaming outward from a sharp neutrinosphere at  $r = R_{\nu}$ . The conventional neutrinosphere is defined as the surface outside which the neutrino optical depth is  $2/3$ . Consequently, a significant amount of scattering and emission still occurs at  $r = R_{\nu}$ , giving rise to a significant neutrino flux that is propagating inward as shown in Fig. 4(a) for  $\nu_e$  at  $t_{\text{pb}} = 1.025$  s in our supernova model. In this figure and hereafter, we use  $u \equiv \cos \theta$  to represent the angle of propagation  $\theta$  with respect to the radial direction at radius  $r$  ( $u < 0$  for inward-propagating neutrinos). For our calculations of supernova neutrino flavor evolution, we start from a decoupling sphere at  $r = R_d$  where all inward-propagating neutrino fluxes are negligible ( $\lesssim 2\%$  of the corresponding outward-propagating fluxes in general). As an example to justify our choice of  $R_d$ , we show the luminosities (corrected for gravitational redshift) for different neutrino flavors at  $t_{\text{pb}} = 1.025$  s as functions of radius in Fig. 4(b). It can be seen that all luminosities stay constant at  $r > R_d$  to very good approximation.

We employ the neutrino energy and angular distributions  $f_{\nu}(t_{\text{em}}, E, u_d, R_d)$  at  $r = R_d$  (with  $u_d \equiv \cos \theta_d$ ) from our supernova model, which change significantly over  $\sim 10$  s as illustrated by the evolution of average neutrino energies in Fig. 2. We emphasize that it is important to use realistic neutrino energy and angular distributions at emission in

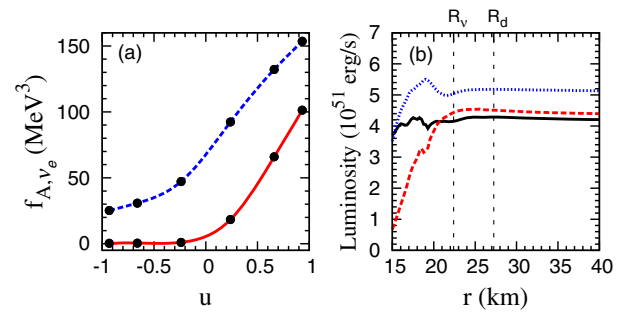


FIG. 4 (color online). Neutrino decoupling in the  $18M_{\odot}$  supernova model. (a) Comparison of  $\nu_e$  angular distributions at the conventional neutrinosphere ( $r = R_{\nu}$ , blue dashed curve) and the decoupling sphere ( $r = R_d$ , red solid curve) for  $t_{\text{pb}} = 1.025$  s. (b) Luminosities (corrected for gravitational redshift) of  $\nu_e$  (black solid curve),  $\bar{\nu}_e$  (red dashed curve), and  $\nu_{\mu(\tau)}$  (blue dotted curve) as functions of radius for  $t_{\text{pb}} = 1.025$  s, exhibiting constancy at  $r > R_d$  to very good approximation. The luminosity of  $\bar{\nu}_{\mu(\tau)}$  is essentially the same as that of  $\nu_{\mu(\tau)}$ .



calculating supernova neutrino flavor evolution, especially the collective oscillations. In particular, we note that in contrast to the isotropic emission typically assumed in previous studies of collective oscillations, realistic neutrino angular distributions are forward peaked as shown for  $\nu_e$  in Fig. 4(a). The effects of  $f_\nu(t_{\text{em}}, E, u_d, R_d)$  on collective neutrino oscillations will be discussed in Sec. IV A.

In the absence of neutrino oscillations, the neutrino distributions at  $r > R_d$  are given by

$$f_\nu(t_{\text{em}}, E, u, r) = f_\nu(t_{\text{em}}, E, u_d, R_d), \quad (2)$$

where  $u$  and  $u_d$  (see Fig. 1) are related by

$$u = \sqrt{1 - (R_d/r)^2(1 - u_d^2)}. \quad (3)$$

The corresponding neutrino number density distributions per unit energy interval per unit solid angle at  $r > R_d$  are given by

$$\frac{d^2 n_\nu}{dE d\Omega} = \frac{E^2}{(2\pi)^3} f_\nu(t_{\text{em}}, E, u, r), \quad (4)$$

where  $d\Omega \equiv d\theta d\phi$  with  $\phi$  being the azimuthal angle. In the above equation and elsewhere in the paper, natural units with  $\hbar = c = 1$  are used.

The neutrino number density distributions in Eq. (4) have azimuthal symmetry around the radial direction. We assume that this symmetry also applies to neutrino flavor evolution at  $r > R_d$ , where neutrinos experience forward scattering on other neutrinos and on electrons. The latter have a spherically symmetric number density profile  $n_e(r)$  in our supernova model. Under the above assumption, the wave function  $\psi_\nu(t_{\text{em}}, E, u, r)$  for a neutrino emitted with energy  $E$  at time  $t_{\text{em}}$  and arriving at radius  $r$  with a propagation angle specified by  $u$  satisfies a Schrödinger-like equation,

$$i \frac{d\psi_\nu}{dt} = (H_\nu + H_e + H_\nu) \psi_\nu(t_{\text{em}}, E, u, r), \quad (5)$$

where  $H_\nu$ ,  $H_e$ , and  $H_\nu$  are the effective Hamiltonians due to vacuum neutrino masses, neutrino-electron forward scattering [11], and neutrino-neutrino forward scattering [47–49], respectively. In our rotated flavor basis  $(|\nu_e\rangle, |\nu_x\rangle, |\nu_y\rangle)^T$ , the wave function is  $\psi_\nu(t_{\text{em}}, E, u, r) = (a_e, a_x, a_y)^T$ , where  $a_e$ ,  $a_x$ , and  $a_y$  are the amplitudes for being a  $\nu_e$ ,  $\nu_x$ , and  $\nu_y$ , respectively. In the same basis, the effective Hamiltonians are

$$H_\nu = U \frac{M^2}{2E} U^\dagger, \quad (6a)$$

$$H_e = \sqrt{2} G_F n_e(r) \text{diag}(1, 0, 0), \quad (6b)$$

$$H_\nu = \sqrt{2} G_F \sum_\alpha \int dE' d\Omega' (1 - uu') \times \left[ \frac{d^2 n_{\nu_\alpha}}{dE' d\Omega'} \rho_{\nu_\alpha}(t'_{\text{em}}, E', u', r) - \frac{d^2 n_{\bar{\nu}_\alpha}}{dE' d\Omega'} \rho_{\bar{\nu}_\alpha}^*(t'_{\text{em}}, E', u', r) \right]. \quad (6c)$$

In the above equations,  $M = \text{diag}(m_1, m_2, m_3)$ ,  $U = R_{13}(\theta_{13})R_{12}(\theta_{12})$ ,  $n_e = \rho Y_e N_A$  with  $N_A$  being Avogadro's number,  $\rho_{\nu_\alpha} = \psi_{\nu_\alpha} \psi_{\nu_\alpha}^\dagger$ , and  $\alpha = \{e, x, y\}$  denotes the initial neutrino flavor.

The nonlinear coupling among all neutrinos introduced by  $H_\nu$  can lead to collective oscillations (see [13] for a review and [14–36] for more recent developments). To estimate the relative importance of  $H_e$  and  $H_\nu$  for our supernova model, we show in Fig. 5 the profiles of  $n_e(r)$  and the net  $\nu_e$  number density  $n_{\nu_e}(r) - n_{\bar{\nu}_e}(r)$  in the absence of neutrino oscillations for  $t_{\text{pb}} \approx 0.6, 1.0,$  and  $3.0$  s, respectively. It can be seen that  $n_{\nu_e} - n_{\bar{\nu}_e}$  can exceed  $n_e$  for some radii only at  $t_{\text{pb}} \gtrsim 1.0$  s. Recent studies [17,34,50] suggest that for  $n_{\nu_e} - n_{\bar{\nu}_e} \ll n_e$ , collective oscillations are suppressed due to large dispersion in  $H_e$  for neutrinos with different propagation angles. Consequently, we expect that collective oscillations are suppressed for  $t_{\text{pb}} < 1.0$  s, i.e., during the accretion phase and the very early cooling phase in our supernova model. We focus our numerical calculations of neutrino flavor evolution on the period of  $0.6 \lesssim t_{\text{pb}} \lesssim 10.0$  s, during which collective oscillations might occur.

We note that although  $f_\nu(t_{\text{em}}, E, u_d, R_d)$  and  $n_e(r)$  change significantly over  $0.6 \lesssim t_{\text{pb}} \lesssim 10.0$  s, they can be taken as fixed during the time between emission of a neutrino at  $r = R_d$  and its arrival at  $r \lesssim 500$  km, where  $H_\nu$  might drive collective oscillations (see Fig. 5). Therefore,

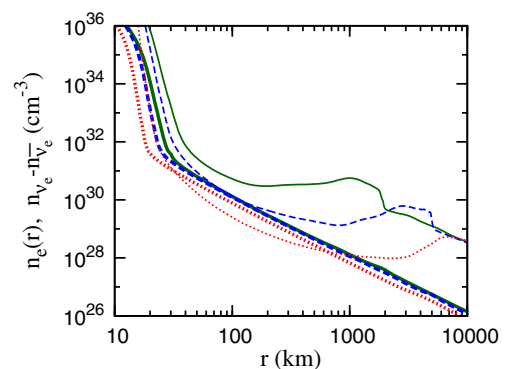


FIG. 5 (color online). Profiles of  $n_e(r)$  (thin curves) and the net  $\nu_e$  number density  $n_{\nu_e}(r) - n_{\bar{\nu}_e}(r)$  in the absence of neutrino oscillations (thick curves) for  $t_{\text{pb}} \approx 0.6$  (green solid curve),  $1.0$  (blue dashed curve), and  $3.0$  s (red dotted curve), respectively, in the  $18M_\odot$  supernova model.

in solving Eq. (5), we first consider a snapshot of  $f_\nu(t_{\text{em}}, E, u_d, R_d)$  and  $n_e(r)$  for a specific  $t_{\text{em}}$ , and then use the corresponding  $H_\nu$  and  $H_e$  to evolve  $\psi_\nu(t_{\text{em}}, E, u, r)$  at  $r > R_d$ . A total of  $\approx 50$  snapshots are taken to cover  $0.6 \lesssim t_{\text{pb}} \lesssim 10.0$  s. For each snapshot, we map  $f_\nu(t_{\text{em}}, E, u_d, R_d)$  from our supernova model onto a grid of  $E$  and  $v \equiv u_d^2$ . As  $u = \sqrt{1 - (R_d/r)^2(1 - v)}$  [see Eq. (3)], the dependence on  $u$  is equivalent to that on  $v$ . Using  $dt = dr/u$  (see Fig. 1), we can rewrite Eq. (5) as

$$i \frac{d\psi_\nu}{dr} = \left( \frac{H_\nu + H_e}{u} + H'_\nu \right) \psi_\nu(t_{\text{em}}, E, v, r), \quad (7)$$

where

$$H'_\nu = \pi \sqrt{2} G_F \left( \frac{R_d}{r} \right)^2 \sum_\alpha \int dE' dv' \left( \frac{1}{uu'} - 1 \right) \times \left[ \frac{d^2 n_{\nu_\alpha}}{dE' d\Omega'} \rho_{\nu_\alpha}(t_{\text{em}}, E', v', r) - \frac{d^2 n_{\bar{\nu}_\alpha}}{dE' d\Omega'} \rho_{\bar{\nu}_\alpha}^*(t_{\text{em}}, E', v', r) \right]. \quad (8)$$

The evolution equation for  $\psi_{\bar{\nu}}(t_{\text{em}}, E, v, r)$  can be obtained by the substitution  $H_e \rightarrow -H_e$  and  $H'_\nu \rightarrow -(H'_\nu)^*$  in Eq. (7). The results for  $\psi_\nu(t_{\text{em}}, E, v, r)$  and  $\psi_{\bar{\nu}}(t_{\text{em}}, E, v, r)$  are presented in Sec. IV.

#### IV. RESULTS ON COLLECTIVE NEUTRINO OSCILLATIONS

By solving Eq. (7), we find that no significant neutrino flavor evolution occurs at  $r \leq 500$  km in our supernova model for the normal mass hierarchy, and that collective neutrino oscillations of particular interest to us have already ceased at  $r = 500$  km for the inverted mass hierarchy. We focus on the latter case and present the corresponding results at  $r \leq 500$  km for  $0.6 \lesssim t_{\text{pb}} \lesssim 10.0$  s in this section. We define the angle-averaged survival probability of  $\nu_e$  as

$$\langle P_{\nu_e \nu_e} \rangle_v \equiv \frac{\int P_{\nu_e \nu_e}(t_{\text{em}}, E, v, r) f_{\nu_e}(t_{\text{em}}, E, u, r) du}{\int f_{\nu_e}(t_{\text{em}}, E, u, r) du}, \quad (9a)$$

$$= \frac{\int P_{\nu_e \nu_e}(t_{\text{em}}, E, v, r) f_{\nu_e}(t_{\text{em}}, E, u_d, R_d) dv/u}{\int f_{\nu_e}(t_{\text{em}}, E, u_d, R_d) dv/u}, \quad (9b)$$

where we have used  $f_{\nu_e}(t_{\text{em}}, E, u, r) = f_{\nu_e}(t_{\text{em}}, E, u_d, R_d)$  [Eq. (2)],  $v = u_d^2$ , and  $u = \sqrt{1 - (R_d/r)^2(1 - v)}$  [Eq. (3)] to give the second expression. We show  $\langle P_{\nu_e \nu_e} \rangle_v$  and  $\langle P_{\bar{\nu}_e \bar{\nu}_e} \rangle_v$  as functions of  $t_{\text{em}}$  and  $E$  for  $r = 500$  km in Fig. 6 and summarize these results below:

- (1) For  $t_{\text{pb}} \lesssim 0.8$  s, collective oscillations are suppressed by the large  $H_e$  as expected;
- (2) For  $0.8 < t_{\text{pb}} \lesssim 1.5$  s, significant flavor conversion occurs for neutrinos with  $E \gtrsim 8$  MeV and for most antineutrinos;
- (3) For  $1.5 < t_{\text{pb}} \lesssim 5.0$  s, only neutrinos with  $10 \lesssim E \lesssim 20$  MeV undergo collective oscillations;
- (4) For  $t_{\text{pb}} > 5.0$  s, collective oscillations are highly suppressed for all neutrinos and antineutrinos, and flavor conversion of low-energy  $\bar{\nu}_e$  at these late times is driven by  $H_e$  through the adiabatic MSW effect.

The effective neutrino energy spectra at  $r = 500$  km can be obtained from the survival probabilities shown in Fig. 6. In addition, it is important to examine the detailed neutrino flavor evolution at  $r < 500$  km so that its effects on physical processes at these radii can be assessed. We define the angle-and-energy-averaged probability for conversion of an initial  $\nu_e$  into a  $\nu_x$  as

$$\langle P_{\nu_e \nu_x} \rangle_{v,E} \equiv \frac{\int P_{\nu_e \nu_x}(t_{\text{em}}, E, v, r) E^2 f_{\nu_e}(t_{\text{em}}, E, u, r) dE du}{\int E^2 f_{\nu_e}(t_{\text{em}}, E, u, r) dE du}, \quad (10a)$$

$$= \frac{\int P_{\nu_e \nu_x}(t_{\text{em}}, E, v, r) E^2 f_{\nu_e}(t_{\text{em}}, E, u_d, R_d) dE dv/u}{\int E^2 f_{\nu_e}(t_{\text{em}}, E, u_d, R_d) dE dv/u}. \quad (10b)$$

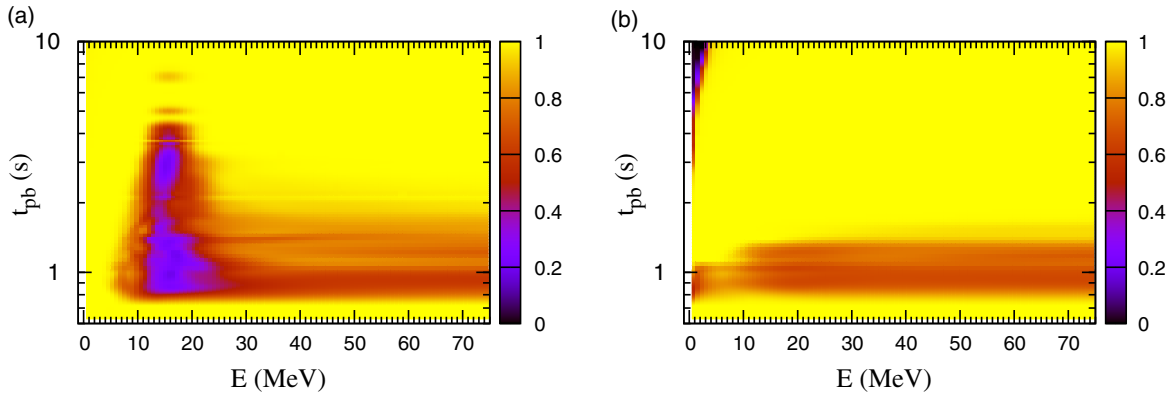


FIG. 6 (color online). The angle-averaged survival probabilities (a)  $\langle P_{\nu_e \nu_e} \rangle_v$  and (b)  $\langle P_{\bar{\nu}_e \bar{\nu}_e} \rangle_v$  as functions of  $E$  and emission time  $t_{\text{em}}$  (in terms of  $t_{\text{pb}}$ ) at  $r = 500$  km.

The thick curves in Fig. 7 show  $\langle P_{\nu_e\nu_x} \rangle_{v,E}$ ,  $\langle P_{\nu_e\nu_y} \rangle_{v,E}$ ,  $\langle P_{\bar{\nu}_e\bar{\nu}_x} \rangle_{v,E}$ , and  $\langle P_{\bar{\nu}_e\bar{\nu}_y} \rangle_{v,E}$  as functions of radius for  $t_{\text{pb}} = 1.025, 3.007, \text{ and } 5.0$  s, respectively.

In general, the growth of  $\langle P_{\nu_e\nu_y} \rangle_{v,E}$  ( $\langle P_{\bar{\nu}_e\bar{\nu}_y} \rangle_{v,E}$ ) corresponds to flavor conversion between  $\nu_e$  ( $\bar{\nu}_e$ ) and  $\nu_y$  ( $\bar{\nu}_y$ ) in the 1–3 subspace associated with the larger mass-squared difference  $|\Delta m_{31}^2|$ , while that of  $\langle P_{\nu_e\nu_x} \rangle_{v,E}$  and  $\langle P_{\bar{\nu}_e\bar{\nu}_x} \rangle_{v,E}$

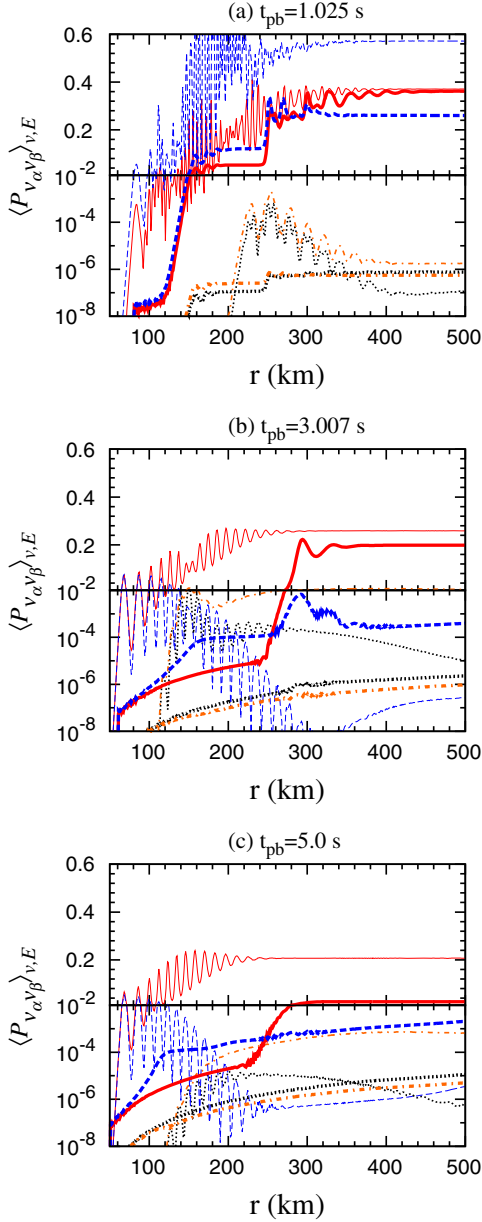


FIG. 7 (color online). Angle- and energy-averaged conversion probabilities  $\langle P_{\nu_e\nu_x} \rangle_{v,E}$  (thick black dotted curve),  $\langle P_{\nu_e\nu_y} \rangle_{v,E}$  (thick red solid curve),  $\langle P_{\bar{\nu}_e\bar{\nu}_x} \rangle_{v,E}$  (thick orange dash-dotted curve), and  $\langle P_{\bar{\nu}_e\bar{\nu}_y} \rangle_{v,E}$  (thick blue dashed curve) as functions of radius calculated from multi-angle simulations for  $t_{\text{pb}} = 1.025$  (a), 3.007 (b), and 5.0 s (c). Similar quantities from single-angle calculations are shown as the corresponding thin curves.

corresponds to flavor conversion associated with  $\Delta m_{21}^2$ . Because flavor instabilities, which mark the rapid growth of the flavor conversion probabilities, are greatly suppressed by the multi-angle effects from both  $H_e$  and  $H_\nu$  (e.g., [15,22,50]), large  $e$ - $y$  oscillations occur only at  $r \sim 100$ –300 km and  $e$ - $x$  oscillations are always negligible. Flavor evolution shown in Fig. 7(a) is representative of that for  $0.8 < t_{\text{pb}} \lesssim 1.5$  s, when significant flavor conversion occurs in both the neutrino and antineutrino sectors. In this case, there are two different flavor instabilities occurring at  $r \approx 120$  and 240 km, respectively. The first instability induces more oscillations of antineutrinos, while the second affects neutrinos more. In contrast, there is only one flavor instability affecting mostly neutrinos at  $200 \lesssim r \lesssim 250$  km for  $1.5 < t_{\text{pb}} \lesssim 5$  s (see Figs. 7b and 7c). For these later times, the average conversion probability also grows more slowly to smaller values, and a smaller portion of the neutrino spectrum is affected as shown in Fig. 6(a).

To facilitate further discussion of the above results, we define the vacuum oscillation frequency  $\omega \equiv |\Delta m_{31}^2|/(2E)$  for neutrinos and  $\omega = -|\Delta m_{31}^2|/(2E)$  for antineutrinos. We also define a normalized neutrino energy spectrum as a function of  $\omega$ ,

$$g(\omega) = \frac{|\Delta m_{31}^2|}{2\omega^2} \times \begin{cases} [g_{\nu_e}(E) - g_{\nu_y}(E)], & \text{for } \omega > 0, \\ [g_{\bar{\nu}_y}(E) - g_{\bar{\nu}_e}(E)], & \text{for } \omega < 0, \end{cases} \quad (11)$$

where

$$g_{\nu_\alpha}(E) = \tilde{g}_{\nu_\alpha}(E)/G_\nu, \quad (12a)$$

$$\tilde{g}_{\nu_\alpha}(E) = \int E^2 f_{\nu_\alpha}(t_{\text{em}}, E, u_d, R_d) u_d du_d, \quad (12b)$$

$$G_\nu = \int [\tilde{g}_{\nu_e}(E) - \tilde{g}_{\bar{\nu}_e}(E) - \tilde{g}_{\nu_y}(E) + \tilde{g}_{\bar{\nu}_y}(E)] dE. \quad (12c)$$

In the above equations,  $\tilde{g}_{\nu_\alpha}(E)$ , and hence,  $G_\nu$ ,  $g_{\nu_\alpha}(E)$ , and  $g(\omega)$ , depend on  $t_{\text{em}}$ . This dependence is suppressed for simplicity. Note that  $f_{\nu_y}(t_{\text{em}}, E, u_d, R_d) = f_{\nu_{\mu(\tau)}}(t_{\text{em}}, E, u_d, R_d)$  and  $f_{\bar{\nu}_y}(t_{\text{em}}, E, u_d, R_d) = f_{\bar{\nu}_{\mu(\tau)}}(t_{\text{em}}, E, u_d, R_d)$  in our supernova model. It is also useful to introduce two effective potentials

$$\lambda(r) = \sqrt{2} G_F n_e(r) \frac{R_d^2}{2r^2}, \quad (13a)$$

$$\mu(r) = \sqrt{2} G_F \left( \frac{G_\nu}{2\pi^2} \right) \frac{R_d^4}{4r^4}, \quad (13b)$$

which approximately represent the differences in  $H_e$  and  $H_\nu$  among neutrinos with different propagation angles, and can be used to measure the so-called ‘‘multi-angle’’ effects on collective oscillations [22]. As the net neutrino number density at radius  $r$  is  $\sim n_{\nu_e} - n_{\bar{\nu}_e} \sim [G_\nu/(2\pi^2)] R_d^2/(2r^2)$ ,

comparing  $\lambda(r)$  and  $\mu(r)$  is roughly equivalent to comparing  $n_e$  and  $n_{\nu_e} - n_{\bar{\nu}_e}$  (see Fig. 5).

### A. Multi-angle effects on flavor evolution

The above results on collective neutrino oscillations are obtained from the so-called ‘‘multi-angle’’ simulations in contrast to the ‘‘single-angle’’ approximation, which assumes that neutrino flavor evolution is independent of the propagation angle (e.g., [44]). The single-angle approximation was widely used in the literature to facilitate analytical understanding of collective oscillations. In some cases, the results from this approximation qualitatively agree with those from multi-angle simulations. Examples include cases where fluxes of  $\nu_{\mu(\tau)}$  and  $\bar{\nu}_{\mu(\tau)}$  are significantly smaller than those of  $\nu_e$  and  $\bar{\nu}_e$  [19,44,51] and the case of the neutronization burst of an O-Ne-Mg core-collapse supernova [52–54]. However, for neutrino energy spectra representative of the cooling phase, the results from multi-angle simulations are typically very different from those obtained with the single-angle approximation [15,55,56]. Below we compare the multi-angle and single-angle results for our supernova model.

We perform single-angle calculations assuming that neutrinos are emitted uniformly within the forward  $2\pi$  solid angle at  $r = R_d$  with the same total fluxes and energy spectra as given by our supernova model and that neutrinos with the same energy undergo the same flavor evolution at  $r > R_d$  as those propagating radially. The resulting energy-averaged conversion probabilities  $\langle P_{\nu_e\nu_e} \rangle_E$ ,  $\langle P_{\nu_e\nu_x} \rangle_E$ ,  $\langle P_{\bar{\nu}_e\bar{\nu}_x} \rangle_E$ , and  $\langle P_{\bar{\nu}_e\bar{\nu}_y} \rangle_E$  as functions of radius are shown as thin curves in Fig. 7 for  $t_{\text{pb}} = 1.025, 3.007,$  and  $5.0$  s, respectively. It can be seen that there is rapid growth of  $\langle P_{\nu_e\nu_y} \rangle_E$  and  $\langle P_{\bar{\nu}_e\bar{\nu}_y} \rangle_E$  at  $r < 100$  km in all cases. This early onset of flavor oscillations is due to a flavor instability that occurs in an isotropic environment when there is multiple spectral crossings corresponding to  $g(\omega) = 0$  even for arbitrarily large electron and/or neutrino density [55]. This instability also triggers the onset of  $e-x$  conversion in the region of collective oscillations [57,58]. In contrast, neutrinos with different propagation angles experience different histories of  $H_e$  and  $H_\nu$  in multi-angle calculations. This greatly suppresses flavor instabilities, with large  $e-y$  oscillations occurring only at  $r \sim 100\text{--}300$  km and  $e-x$  oscillations being always negligible (see Fig. 7).

The most distinct feature of collective oscillations is that  $\nu_e$  and  $\bar{\nu}_e$  can swap part of their spectra with  $\nu_{\mu,\tau}$  and  $\bar{\nu}_{\mu,\tau}$  [44,51,55–57]. Such spectral splits or swaps are best illustrated by the probabilities  $1 - P_{\nu_e\nu_y}$  and  $1 - P_{\bar{\nu}_e\bar{\nu}_y}$  at  $r = 500$  km as functions of  $\omega$  obtained from the single-angle calculations, which are shown as the blue dashed curve in Fig. 8 for  $t_{\text{pb}} = 1.025, 3.007,$  and  $5.0$  s, respectively. The function  $g(\omega)/15 + 0.5$  is shown as the green dotted curve in the same figure and indicates that spectral splits or swaps could form around the ‘‘positive’’ spectral

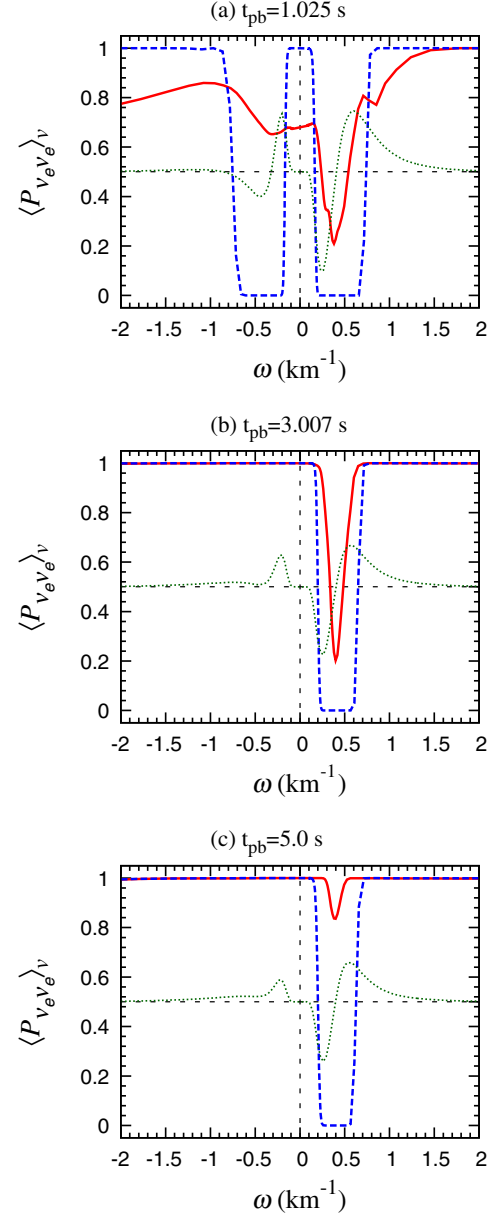


FIG. 8 (color online). Angle-averaged survival probabilities  $\langle P_{\nu_e\nu_e} \rangle_v$  ( $\omega > 0$ ) and  $\langle P_{\bar{\nu}_e\bar{\nu}_e} \rangle_v$  ( $\omega < 0$ ) at  $r = 500$  km as functions of  $\omega$  calculated from multi-angle simulations (red solid curve) for  $t_{\text{pb}} = 1.025$  (a),  $3.007$  (b), and  $5.0$  s (c). The corresponding single-angle results for  $1 - P_{\nu_e\nu_y}$  and  $1 - P_{\bar{\nu}_e\bar{\nu}_y}$  are shown as blue dashed curves. The green dotted curves give the function  $g(\omega)/15 + 0.5$ .

crossings corresponding to  $g(\omega) = 0$  and  $dg/d\omega > 0$  under the single-angle approximation [55]. However, because neutrinos with different propagation angles experience different  $H_\nu$  in multi-angle calculations, different parts of their energy spectra are in resonance when flavor instabilities or large-scale flavor oscillations occur (e.g., [19]). Consequently, the splits in their energy spectra are generally smoothed out when averaged over the propagation angle. This can be seen from the angle-averaged



survival probabilities  $\langle P_{\nu_e \nu_e} \rangle_v$  and  $\langle P_{\bar{\nu}_e \bar{\nu}_e} \rangle_v$  at  $r = 500$  km as functions of  $\omega$ , which are shown as the red solid curve in Fig. 8. Note that  $\langle P_{\nu_e \nu_e} \rangle_v \approx 1 - \langle P_{\nu_e \nu_y} \rangle_v$  and  $\langle P_{\bar{\nu}_e \bar{\nu}_e} \rangle_v \approx 1 - \langle P_{\bar{\nu}_e \bar{\nu}_y} \rangle_v$  because  $\langle P_{\nu_e \nu_x} \rangle_v$  and  $\langle P_{\bar{\nu}_e \bar{\nu}_x} \rangle_v$  are negligible in multi-angle calculations (see Fig. 7).

We also note that flavor conversion of antineutrinos occurs only when there is an excess of  $\bar{\nu}_e$  over  $\bar{\nu}_y$ , i.e.,  $g(\omega) < 0$ , for some range of  $\omega < 0$ . This is demonstrated in Fig. 8(a) for  $t_{\text{pb}} = 1.025$  s with  $g(\omega) < 0$  for  $-0.9 \lesssim \omega \lesssim -0.3$  km $^{-1}$  ( $7 \lesssim E \lesssim 19$  MeV), which is representative of the early deleptonization phase during protoneutron star evolution. At later times, the energy spectra of  $\bar{\nu}_e$  and  $\bar{\nu}_y$  become similar but the luminosity of  $\bar{\nu}_y$  remains higher than that of  $\bar{\nu}_e$ . This results in  $g(\omega) > 0$  for all  $\omega < 0$  as shown for  $t_{\text{pb}} = 3.007$  and 5.0 s in Figs. 8(b) and 8(c), respectively. There is only one positive spectral crossing at  $\omega > 0$ , i.e., in the neutrino sector, at these later times. Consequently, only the spectra of neutrinos are affected by collective oscillations [see Figs. 8(b) and 8(c)].

To conclude this subsection, we examine the effects of neutrino angular distributions on flavor evolution in supernovae using multi-angle simulations. As shown in Fig. 4, the neutrino distributions  $f(t_{\text{em}}, E, u_d, R_d)$  at the decoupling sphere are strongly forward-peaked instead of being isotropic as often assumed in earlier studies of collective oscillations. Compared to a physical forward-peaked neutrino angular distribution, the crude assumption of isotropic neutrino emission leads to artificially larger  $H_\nu$  for any specific neutrino trajectory because of the larger contributions from the more tangentially-emitted neutrinos. In Fig. 9, we show the angle-averaged survival probability  $\langle P_{\nu_e \nu_e} \rangle_v$  as a function of  $\omega$  at  $t_{\text{pb}} = 1.025$  s (blue dashed curve) obtained from multi-angle calculations with the same total neutrino fluxes and energy spectra as given by our supernova model but assuming isotropic neutrino

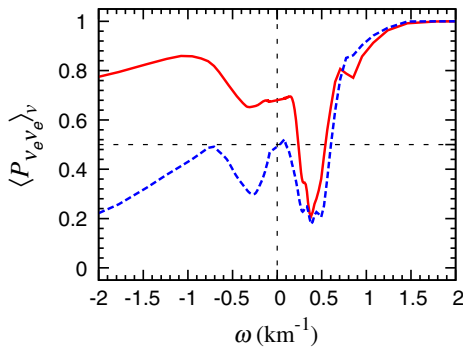


FIG. 9 (color online). Angle-averaged survival probabilities  $\langle P_{\nu_e \nu_e} \rangle_v$  ( $\omega > 0$ ) and  $\langle P_{\bar{\nu}_e \bar{\nu}_e} \rangle_v$  ( $\omega < 0$ ) as functions of  $\omega$  at  $r = 500$  km for  $t_{\text{pb}} = 1.025$  s obtained from multi-angle simulations assuming isotropic neutrino emission (blue dashed curve). The red solid curve [same as in Fig. 8(a)] is calculated with the forward-peaked neutrino angular distributions in our supernova model and is shown for comparison.

emission. Compared with the result based on the neutrino angular distributions in our supernova model (red solid curve), the unphysical isotropic angular distribution gives much smaller survival probabilities for antineutrinos ( $\omega < 0$ ). It also causes the onset of flavor oscillations to occur at smaller radii. We emphasize that it requires not only multi-angle simulations, but also the use of proper neutrino angular distributions to accurately treat collective neutrino oscillations in supernovae.

## B. Flavor instabilities and effects of $n_e$

As mentioned above, there are two different flavor instabilities occurring at  $r \approx 120$  and 240 km, respectively, for collective neutrino oscillations shown in Fig. 7(a), which are representative of the epoch of  $0.8 < t_{\text{pb}} \lesssim 1.5$  s. In contrast, there is only one flavor instability occurring at  $200 \lesssim r \lesssim 250$  km for  $1.5 < t_{\text{pb}} \lesssim 5$  s [see Figs. 7(b) and 7(c)]. Using the detailed results from our multi-angle simulations, we show the radius  $r_{\text{on}}$  for the onset of either instability as a function of time in Fig. 10(a). The corresponding  $\lambda_{\text{on}} = \lambda(r_{\text{on}})$  and  $\mu_{\text{on}} = \mu(r_{\text{on}})$  are shown in Fig. 10(b). The instability occurring at smaller radii is tied to the substantial excess of  $\bar{\nu}_e$  over  $\bar{\nu}_y$  for some energy range [e.g.,  $g(\omega) < 0$  for  $-0.9 \lesssim \omega \lesssim -0.3$  km $^{-1}$  in Fig. 8(a)] characteristic of the early deleptonization epoch at  $t_{\text{pb}} \sim 1.0$  s. The corresponding values of  $\lambda_{\text{on}} \sim \mu_{\text{on}} \sim 10$  km $^{-1}$  are much larger than the typical spread in  $\omega$  of  $\Delta\omega \sim 0.6$  km $^{-1}$ . In contrast, the instability occurring at larger radii exists for  $t_{\text{pb}} \gtrsim 1.0$  s because there is always an excess of  $\nu_e$  over  $\nu_y$  for some energy range [see Figs. 8(a) and 8(b)]. This instability generally corresponds to  $\mu_{\text{on}} \sim \Delta\omega$ .

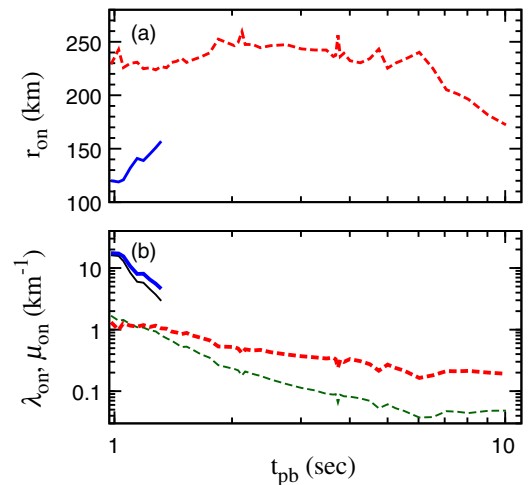


FIG. 10 (color online). (a) Onset radii  $r_{\text{on}}$  for two flavor instabilities as functions of time. (b) Corresponding  $\lambda_{\text{on}} = \lambda(r_{\text{on}})$  (thin curves) and  $\mu_{\text{on}} = \mu(r_{\text{on}})$  (thick curves) as functions of time. The instability occurring at smaller radii (solid curves) only exists for  $t_{\text{pb}} \sim 1$  s while that occurring at larger radii (dashed curves) exists for  $t_{\text{pb}} \gtrsim 1$  s.

As mentioned at the beginning of Sec. IV, there are no significant collective oscillations at  $t_{\text{pb}} > 5$  s. This is puzzling because there is still a flavor instability occurring at  $r \sim 200$  km for such times (see Fig. 10). We show below that this instability is suppressed by the effects of  $n_e$ , and therefore, fails to cause significant collective oscillations at  $t_{\text{pb}} > 5$  s. We perform multi-angle simulations with modified profiles of electron number density  $n'_e(r) = 0.5n_e(r)$  and  $n''_e(r) = 0.2n_e(r)$  at  $r > R_d$ , respectively, for  $t_{\text{pb}} = 5$  s. We compare the corresponding  $\langle P_{\nu_e\nu_y} \rangle_{v,E}$  as functions of radius with the results calculated for the unmodified  $n_e(r)$  in Fig. 11(b). It can be seen that as  $n_e(r)$  is reduced to  $n'_e(r)$  and then to  $n''_e(r)$ , the onset of flavor instability is pushed to smaller and smaller radii and its growth causes more and more flavor conversion. Therefore, collective oscillations are suppressed by larger  $n_e$ . This generally holds for most of the cooling phase when there is only one flavor instability at  $r \sim 200$  km. We also note that larger  $n_e$  decreases the local effective mixing angle, which tends to reduce flavor conversion similar to the case of a small vacuum mixing angle.

For completeness, we compare  $\langle P_{\nu_e\nu_y} \rangle_{v,E}$  calculated for  $n_e(r)$ ,  $n'_e(r)$ , and  $n''_e(r)$  as functions of radius for  $t_{\text{pb}} = 1.025$  s in Fig. 11(a). It can be seen that in the case of  $n_e(r)$ , the flavor instability at smaller radii stops growing when flavor conversion is still small and a second instability clearly occurs at larger radii. As  $n_e(r)$  is reduced to  $n'_e(r)$  and  $n''_e(r)$ , the “first” instability at  $r \approx 150$  km grows to cause large flavor conversion and a “second” instability can no longer be identified clearly. We also compare  $\langle P_{\nu_e\nu_e} \rangle_v$  and  $\langle P_{\bar{\nu}_e\bar{\nu}_e} \rangle_v$  at  $r = 500$  km calculated for  $n_e(r)$ ,  $n'_e(r)$ , and  $n''_e(r)$  as functions of  $\omega$  for  $t_{\text{pb}} = 1.025$  and 5.0 s in Figs. 12a and 12b, respectively. It can be seen that as  $n_e(r)$  is reduced to  $n'_e(r)$  and then to  $n''_e(r)$ , features of spectral swaps are increasingly sharpened and approach closer and closer to the corresponding results for the single-angle approximation shown in Figs. 8(a) and 8(c).

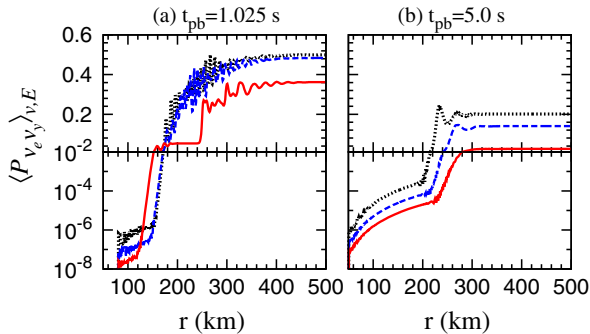


FIG. 11 (color online). Comparison of  $\langle P_{\nu_e\nu_y} \rangle_{v,E}$  calculated for  $n_e(r)$  in our supernova model (red solid curves),  $n'_e(r) = 0.5n_e(r)$  (blue dashed curves), and  $n''_e(r) = 0.2n_e(r)$  (black dotted curves) for  $t_{\text{pb}} = 1.025$  (a) and 5.0 s (b), respectively.

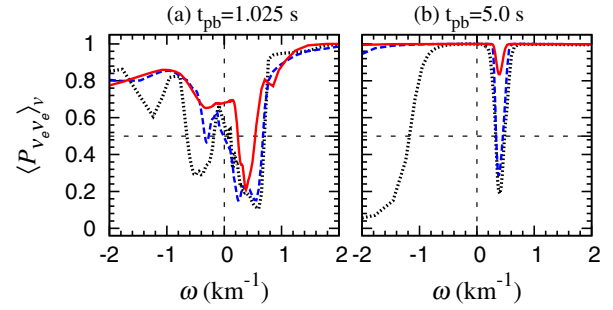


FIG. 12 (color online). Comparison of  $\langle P_{\nu_e\nu_y} \rangle_v$  ( $\omega > 0$ ) and  $\langle P_{\bar{\nu}_e\bar{\nu}_e} \rangle_v$  ( $\omega < 0$ ) at  $r = 500$  km calculated for  $n_e(r)$  in our supernova model (red solid curves),  $n'_e(r) = 0.5n_e(r)$  (blue dashed curves), and  $n''_e(r) = 0.2n_e(r)$  (black dotted curves) for  $t_{\text{pb}} = 1.025$  (a) and 5.0 s (b), respectively. Note that in (b), the  $\bar{\nu}_e$  flavor conversion for  $\omega \lesssim -1$  km $^{-1}$  is due to the MSW effect for the reduced  $n''_e(r)$ .

### C. Results for measured $\theta_{13}$

Recent measurement of  $\bar{\nu}_e$  disappearance by the Daya Bay experiment gave  $\sin^2 2\theta_{13} = 0.092 \pm 0.016 \pm 0.005$  [43], which corresponds to a central value of  $\theta_{13} = 0.15$  that is somewhat larger than the value of  $\theta_{13} = 0.1$  adopted in the above calculations of neutrino oscillations. We have performed additional simulations for  $\theta_{13} = 0.15$  and confirm that our results on neutrino oscillations do not change significantly. As an example, we compare  $\langle P_{\nu_e\nu_y} \rangle_{v,E}$  for  $\theta_{13} = 0.15$  (red solid curve) and 0.1 (black dashed curve) as functions of radius for  $t_{\text{pb}} = 3.007$  s in Fig. 13(a). It can be seen that the flavor instability occurs at the same place and subsequent flavor evolution is identical for both cases. The only change occurs before the onset of the flavor instability, during which time  $\langle P_{\nu_e\nu_y} \rangle_{v,E}$  is slightly larger for  $\theta_{13} = 0.15$  but is very small anyway. We also show  $\Delta\langle P_{\nu_e\nu_e} \rangle_v \equiv \langle P_{\nu_e\nu_e}(\theta_{13} = 0.15) \rangle_v - \langle P_{\nu_e\nu_e}(\theta_{13} = 0.1) \rangle_v$  at  $r = 500$  km as functions of neutrino energy for  $t_{\text{pb}} = 1.025, 1.401, 3.007,$  and 5.0 s, respectively, in

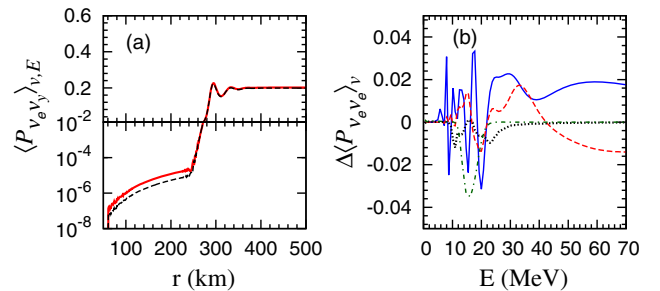


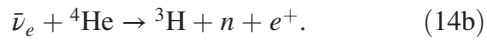
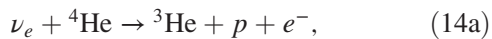
FIG. 13 (color online). (a) Comparison of  $\langle P_{\nu_e\nu_y} \rangle_{v,E}$  for  $\theta_{13} = 0.15$  (red solid curve) and 0.1 (black dashed curve) as functions of radius for  $t_{\text{pb}} = 3.007$  s. (b) Difference in survival probability  $\Delta\langle P_{\nu_e\nu_e} \rangle_v \equiv \langle P_{\nu_e\nu_e}(\theta_{13} = 0.15) \rangle_v - \langle P_{\nu_e\nu_e}(\theta_{13} = 0.1) \rangle_v$  at  $r = 500$  km as functions of neutrino energy for  $t_{\text{pb}} = 1.025$  (blue solid curve), 1.401 (red dashed curve), 3.007 (black dotted curve), and 5.0 s (green dot-dashed curve), respectively.

Fig. 13(b). It can be seen that  $|\Delta\langle P_{\nu_e\nu_e}\rangle_v|$  is  $\lesssim 4\%$  over the entire energy range in all cases. We conclude that our results on neutrino oscillations are insensitive to the exact value of  $\theta_{13}$  and will use those calculated for  $\theta_{13} = 0.1$  to examine the effects on supernova nucleosynthesis and neutrino signals.

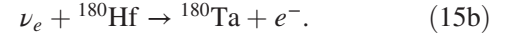
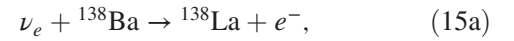
## V. EFFECTS OF NEUTRINO OSCILLATIONS ON NUCLEOSYNTHESIS

Neutrinos play important roles in supernova nucleosynthesis in several major ways and in different locations. For the neutrino-driven wind (see Sec. II) where initially matter is dominantly composed of free nucleons, neutrino reactions (1a) and (1b) set the electron fraction  $Y_e$ , which is a crucial parameter governing the nucleosynthesis in the ejecta. For ejecta with  $Y_e > 0.5$  such as in our supernova model (see Fig. 3), a  $\nu p$  process occurs to produce heavy nuclei during expansion of the mass elements [39,41]. This process requires significant  $\bar{\nu}_e$  absorption on protons when matter evolves through the temperature range of  $T = 1\text{--}3$  GK. In the outer envelope of the star, the interaction of neutrinos with pre-existing nuclei can drive several nucleosynthesis processes including the  $\nu$  process [6,59] and other neutrino-induced nucleosynthesis [5–8]. In the  $\nu$  process, neutrinos can directly transform by charged-current reactions abundant nuclear species into less abundant neighboring nuclei. For example,  $^{138}\text{La}$  and  $^{180}\text{Ta}$  are known to be produced by this mechanism from the abundant  $^{138}\text{Ba}$  and  $^{180}\text{Hf}$  [59,60]. In addition, neutral-current processes excite abundant nuclei to states above particle emission. The decay of these nuclei and subsequent capture of the produced protons, neutrons and/or  $\alpha$  particles contribute to the production of several nuclei including  $^7\text{Li}$ ,  $^{11}\text{B}$ , and  $^{19}\text{F}$ . The production of  $^{19}\text{F}$  is mainly due to neutral-current processes [59] that are not affected by neutrino oscillations. The situation is different for the other species as discussed below.

In the helium shell, neutrinos interact with  $^4\text{He}$  through the charged-current reactions



The  $^3\text{He}$  and  $^3\text{H}$  produced by the above reactions and by neutral-current spallation reactions on  $^4\text{He}$  are important to the production of light nuclei such as  $^7\text{Li}$  and  $^{11}\text{B}$  in the  $\nu$  process through the subsequent reactions  $^3\text{He}(\alpha, \gamma)^7\text{Be}(e^+\nu_e)^7\text{Li}$  and  $^3\text{H}(\alpha, \gamma)^7\text{Li}(\alpha, \gamma)^{11}\text{B}$ . In addition, the neutrons produced by reaction (14b) may lead to a possible neutrino-induced  $r$  process [5,7]. In the O/Ne shell, the production of  $^{138}\text{La}$  and  $^{180}\text{Ta}$  is predominantly determined by the charged-current reactions:



For the above cases, neutrino oscillations can affect nucleosynthesis by changing the energy spectra of  $\nu_e$  and  $\bar{\nu}_e$ , and hence, the rates of charged-current  $\nu_e$  and  $\bar{\nu}_e$  reactions. Many previous studies have discussed the effects of neutrino oscillations on nucleosynthesis in the neutrino-driven wind (e.g., [61,62]) and on the production ratio of  $^7\text{Li}$  to  $^{11}\text{B}$  [63], using time-independent parametrized neutrino spectra and/or ejecta trajectories. Below we apply our results of collective neutrino oscillations, consistently calculated with realistic neutrino emission spectra in a dynamically changing supernova environment as discussed in Sec. IV, to examine the effects of oscillations on the  $\nu p$  process in the neutrino-driven wind, on neutrino-induced nucleosynthesis in helium shells, and on the production of  $^{138}\text{La}$  and  $^{180}\text{Ta}$  by the  $\nu$  process.

### A. Effects on rates of $\nu_e$ and $\bar{\nu}_e$ absorption by free nucleons and the $\nu p$ process

A  $\nu p$  process occurs to produce heavy nuclei during expansion of the mass elements shown in Fig. 3 for our supernova model [41]. This process requires that matter has  $Y_e > 0.5$  and that significant  $\bar{\nu}_e$  absorption by protons occurs when matter evolves through the temperature range of  $3 \gtrsim T \gtrsim 1$  GK. Consequently, an important input is the rates of  $\nu_e$  and  $\bar{\nu}_e$  absorption by free nucleons [reactions (1a) and (1b)]. In the absence of neutrino oscillations, these rates in a mass element reaching radius  $r_m$  at time  $t$  can be calculated as

$$\begin{aligned} \lambda_{\nu N}^0(r_m, t) &= \frac{1}{(2\pi)^2} \int E^2 f_\nu(t, E, u, r_m) \sigma_{\nu N}(E) dE du \quad (16a) \\ &= \frac{R_d^2}{8\pi^2 r_m^2} \int E^2 f_\nu(t, E, u_d, R_d) \sigma_{\nu N}(E) dE dv/u, \end{aligned} \quad (16b)$$

where  $\sigma_{\nu N}$  stands for the absorption cross section  $\sigma_{\nu_e n}$  or  $\sigma_{\bar{\nu}_e p}$  given by

$$\sigma_{\nu_e n}(E) = \sigma_0 \left( \frac{E + \Delta}{\text{MeV}} \right)^2 \left[ 1 + 1.055 \times 10^{-3} \left( \frac{E}{\text{MeV}} \right) \right], \quad (17a)$$

$$\sigma_{\bar{\nu}_e p}(E) = \sigma_0 \left( \frac{E - \Delta}{\text{MeV}} \right)^2 \left[ 1 - 7.669 \times 10^{-3} \left( \frac{E}{\text{MeV}} \right) \right]. \quad (17b)$$

In the above equations,  $\sigma_0 = 0.934 \times 10^{-43} \text{ cm}^2$  and  $\Delta = m_n - m_p = 1.293 \text{ MeV}$  is the neutron-proton mass

difference. These cross sections take into account weak magnetism and nucleon recoil but neglect the electron rest mass  $m_e$  in comparison with  $E$  [64].

The  $\nu p$  process occurs at  $r_m < 10^4$  km [see Fig. 3(a)]. The time for neutrinos to travel from  $r = R_d$  to a mass element at these radii is much shorter than the evolution timescale for the angular and energy distributions of neutrinos at emission. Therefore, we have used  $f_\nu(t, E, u, r_m) = f_\nu(t, E, u_d, R_d)$  in Eq. (16b). The neutrino travel time is also much shorter than the evolution timescale for the profile of  $n_e(r)$ . Consequently, the results on neutrino flavor evolution we have calculated for each time snapshot of our supernova model can be directly applied to obtain the rates of  $\nu_e$  and  $\bar{\nu}_e$  absorption by free nucleons in the presence of neutrino oscillations. These rates can be calculated as, e.g.,

$$\lambda_{\nu_e n}^{\text{osc}}(r_m, t) = \frac{R_d^2}{8\pi^2 r_m^2} \sum_\alpha \int E^2 f_{\nu_\alpha}(t, E, u_d, R_d) \sigma_{\nu_e n}(E) \times P_{\nu_\alpha \nu_e}(t, E, v, r_m) dE dv / u. \quad (18)$$

In Fig. 14, we show  $\lambda_{\nu N}^0(r_m, t)$  and  $\lambda_{\nu N}^{\text{osc}}(r_m, t)/\lambda_{\nu N}^0(r_m, t)$  as functions of  $t - t_0$  for the mass elements that are ejected

from the proto-neutron star at  $t_0 = 0.840, 1.253, 1.726,$  and  $2.526$  s, respectively (both  $t$  and  $t_0$  are in terms of  $t_{\text{pb}}$ ). It can be seen that the overall effect of neutrino oscillations is to enhance both  $\nu_e$  and  $\bar{\nu}_e$  absorption rates. As shown in Fig. 6, flavor conversion mostly takes place between  $\nu_e$  ( $\bar{\nu}_e$ ) and  $\nu_y$  ( $\bar{\nu}_y$ ) with relatively high energies of  $E > 10$  MeV. Because the average  $\nu_y$  ( $\bar{\nu}_y$ ) energy is higher, there are more high-energy  $\nu_y$  ( $\bar{\nu}_y$ ) than  $\nu_e$  ( $\bar{\nu}_e$ ) and the net effect of flavor conversion is to increase the  $\nu_e$  ( $\bar{\nu}_e$ ) absorption rate. In addition, because flavor conversion mostly occurs in the neutrino sector (see Fig. 6), the increase in the  $\nu_e$  absorption rate is larger than that in the  $\bar{\nu}_e$  absorption rate. In the region relevant for the  $\nu p$  process, the effect of flavor conversion on the  $\nu_e$  ( $\bar{\nu}_e$ ) absorption rate also diminishes with time and essentially stops at  $t_{\text{pb}} > 5$  s (1.5 s) as can be seen from Fig. 6. Consequently, the increase in the  $\nu_e$  ( $\bar{\nu}_e$ ) absorption rate due to neutrino oscillations is negligible for the mass elements ejected at  $t_0 > 2.526$  (1.253) s.

We indicate the times at which the temperature of a mass element reaches  $T = 10, 7, 3, 2,$  and  $1$  GK, respectively, in Fig. 14. To affect the setting of  $Y_e$  for a mass element, neutrino oscillations must occur when its temperature is  $T \gtrsim 7$  GK, for which free nucleons dominate its

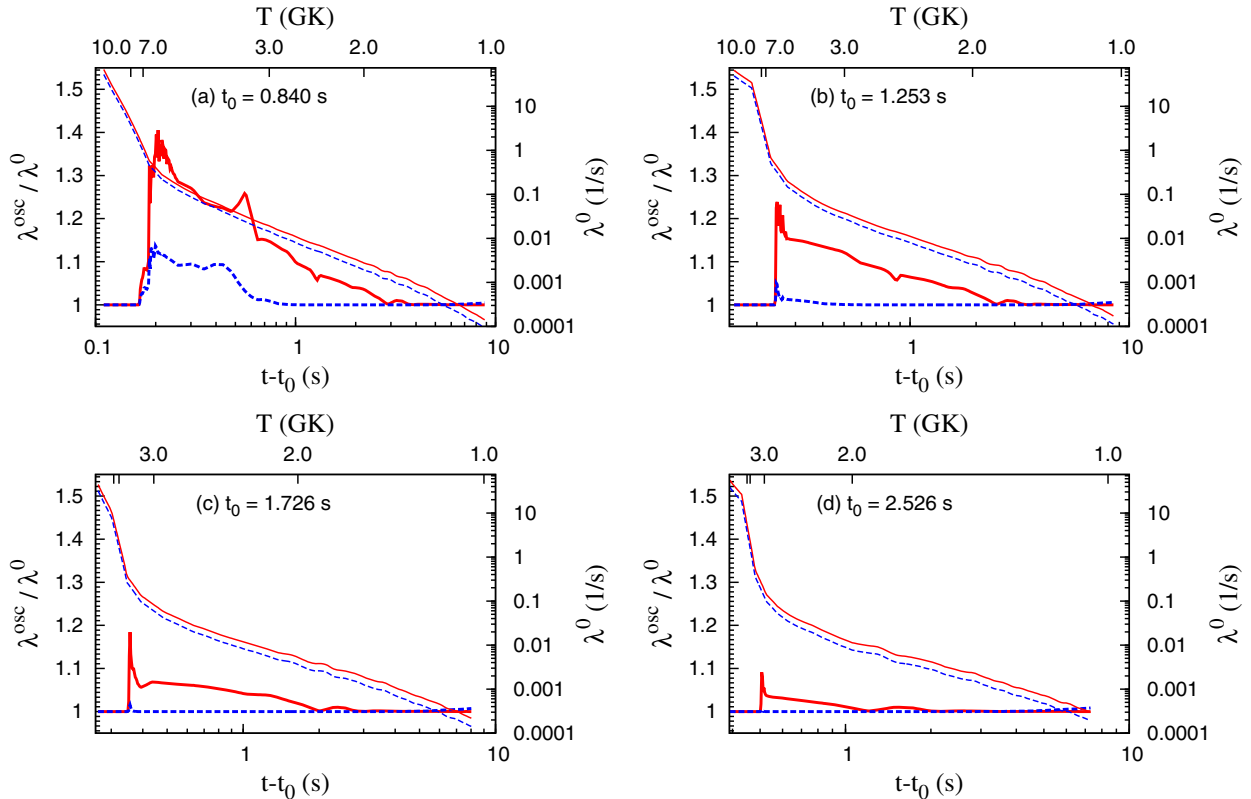


FIG. 14 (color online). Rates  $\lambda_{\nu N}^0$  of  $\nu_e$  (thin solid red curve) and  $\bar{\nu}_e$  (thin dashed blue curve) absorption on free nucleons in the absence of neutrino oscillations as functions of time  $t - t_0$  during expansion of four mass elements ejected from the proto-neutron star at  $t_0 = 0.840$  (a),  $1.253$  (b),  $1.726$  (c), and  $2.526$  s (d), respectively (both  $t$  and  $t_0$  are in terms of  $t_{\text{pb}}$ ). The corresponding thick curves show the ratios  $\lambda_{\nu N}^{\text{osc}}/\lambda_{\nu N}^0$  of absorption rates with and without neutrino oscillations. The times at which the temperature of a mass element reaches  $T = 10, 7, 3, 2,$  and  $1$  GK, respectively, are also indicated.



composition. However, neutrino oscillations start to affect the  $\nu_e$  and  $\bar{\nu}_e$  absorption rates at  $T \lesssim 7$  GK for all the mass elements shown in Fig. 14, and therefore, have little impact on the setting of their  $Y_e$ . The significant increase in the rate of  $\nu_e$  absorption by neutrons at  $T \lesssim 7$  GK does not affect nucleosynthesis because the neutron abundance drops rapidly with decreasing temperature. On the other hand, when the mass elements evolve through the temperature range of  $3 \gtrsim T \gtrsim 1$  GK and  $\bar{\nu}_e$  absorption by protons is instrumental to the ongoing  $\nu p$  process [39], neutrino oscillations have essentially no effect on the  $\bar{\nu}_e$  absorption rate (see Fig. 14). Therefore, the  $\nu p$  process in our supernova model is not affected by neutrino flavor evolution including collective oscillations.

### B. Effects on rates of $\nu_e$ and $\bar{\nu}_e$ absorption by ${}^4\text{He}$ and neutrino-induced nucleosynthesis

The neutrino-induced nucleosynthesis occurs typically in the C/O and He layers of supernovae located at  $r \sim 10^5$  km for massive stars (see Fig. 15). In those layers, the electron number density  $n_e(r)$  is comparable to or less than the MSW resonant density  $n_{e,\text{MSW}}^{(ij)} \equiv (|\Delta m_{ji}^2| \cos 2\theta_{ij}) / (2\sqrt{2}EG_F)$  for relevant neutrino energies of  $\sim 5$ – $100$  MeV. Thus, the detailed neutrino flavor evolution including the MSW effect has to be considered. In our  $18M_\odot$  supernova model, the shock reaches the MSW resonance region and the C/O layer at  $t_{\text{pb}} \approx 5$  s as shown in Fig. 15. We have checked that for  $t_{\text{pb}} < 5$  s, C/O and He layers remain static and the neutrino flavor transformation through the MSW effect is adiabatic, i.e.,  $(\Delta m_{ji}^2 \sin^2 2\theta_{ij}) / (2E \cos 2\theta_{ij}) / |d(\ln n_e)/dr|_{\text{res}} \gg 1$ . The neutrino energy spectra at  $n_e(r) \lesssim n_{e,\text{MSW}}^{(13)}(E)$  can then be calculated as follows.

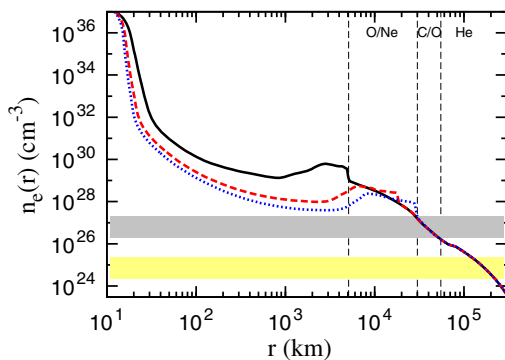


FIG. 15 (color online). Snapshots of the electron number density  $n_e$  as a function of radius for  $t_{\text{pb}} = 1.0$  (black solid curve),  $3.0$  (red dashed curve), and  $5.0$  (blue dotted curve), respectively. The gray and yellow bands indicate the range of  $n_{e,\text{MSW}}^{13}$  and  $n_{e,\text{MSW}}^{12}$  for  $5 < E < 100$  MeV, respectively. The positions of the O/Ne, C/O, and He layers are marked by the vertical lines. The bump in  $n_e$  at  $r \sim 10^3$ – $10^4$  km corresponds to matter that has been shocked recently.

At a radius outside the region of collective oscillations but before the MSW resonances [ $n_e(r) \gg n_{e,\text{MSW}}^{13}(E)$ ], the flavor conversion probability can be approximated by  $P_{\nu_\beta\nu_\alpha}(t, E, u_d, r) \approx P_{\nu_\beta\nu_\alpha}(t, E, u_d, r_f)$ . Here  $r_f$  is the radius where collective neutrino oscillations have ceased. Practically, we take  $r_f = 500$  km. Furthermore, for  $r \gg R_d$ , we can use the approximation  $u \approx 1$ , for which the neutrino interaction rates including the effects of collective oscillations depend on radius only through the geometrical factor  $R_d^2/r^2$  [see e.g., Eq. (18)]. Thus, it is useful to define the angle-integrated neutrino energy spectra,

$$f_{\nu_\alpha}^{(i)}(t, E) \equiv \sum_\beta \int f_{\nu_\beta}(t, E, u_d, R_d) P_{\nu_\beta\nu_\alpha}(t, E, u_d, r_f) u_d du_d, \quad (19)$$

as the radius-independent spectra before neutrinos enter the MSW region of flavor evolution. As these spectra correspond to the region of  $n_e(r) \gg n_{e,\text{MSW}}^{13}(E)$ , where the effective Hamiltonian is nearly diagonal in the flavor basis, the flavor eigenstates  $|\nu_\alpha\rangle$  and the in-medium mass eigenstates  $|\nu_i^m\rangle$  that diagonalize the effective Hamiltonian can be approximately related by  $|\nu_i^m\rangle = \sum_\alpha R_{i\alpha} |\nu_\alpha\rangle$ . For neutrinos, the only nonzero components of  $R_{i\alpha}$  are  $R_{3e} = R_{1x} = R_{2y} = 1$  for the normal mass hierarchy (NH) and  $R_{2e} = R_{1x} = R_{3y} = 1$  for the inverted mass hierarchy (IH). For antineutrinos,  $R_{1e} = R_{2x} = R_{3y} = 1$  ( $R_{3e} = R_{2x} = R_{1y} = 1$ ) are the only nonzero components for the NH (IH).

For adiabatic MSW flavor evolution, neutrinos initially in an in-medium mass eigenstate remain in the corresponding mass eigenstate at later times. As a result, at time  $t$  and radius  $r$ , the neutrino energy spectra including the effects of adiabatic MSW flavor transformation can be written as

$$\begin{aligned} \tilde{f}_{\nu_\alpha}(t, E, r) &= \sum_k \sum_\beta P_{ak}(E, r) R_{k\beta} f_{\nu_\beta}^{(i)}(t', E) \\ &\equiv \sum_\beta P'_{\nu_\alpha\nu_\beta}(E, r) f_{\nu_\beta}^{(i)}(t', E), \end{aligned} \quad (20)$$

where  $P_{ak}(E, r) = |\langle \nu_\alpha | \nu_k^m(E, r) \rangle|^2$  is the probability that the in-medium mass eigenstate  $|\nu_k^m(E, r)\rangle$  at radius  $r$  coincides with the flavor eigenstate  $|\nu_\alpha\rangle$ , and  $P'_{\nu_\alpha\nu_\beta}(E, r) = \sum_k P_{ak}(E, r) R_{k\beta}$  is the effective probability to convert a  $\nu_\beta$  at time  $t' \approx t - r/c$  into a  $\nu_\alpha$  at time  $t$  and radius  $r$  by adiabatic MSW flavor transformation. Note that  $P_{ak}$  is independent of time for  $t_{\text{pb}} < 5.0$  s before the shock arrives in the MSW region of flavor evolution. We numerically derive the in-medium mass eigenstates  $|\nu_k^m(E, r)\rangle$  by diagonalizing  $H_\nu(E) + H_e(r)$  with  $n_e(r)$  from the supernova progenitor model [65]. We show  $P'_{\nu_e\nu_e}$  and  $P'_{\bar{\nu}_e\bar{\nu}_e}$  as functions of  $r$  and  $E$  in Fig. 16.

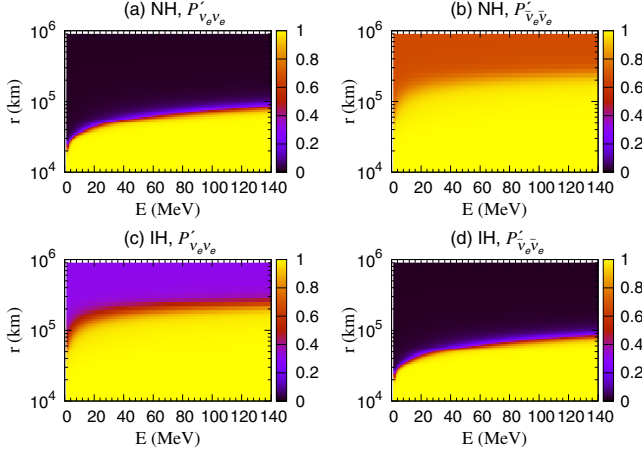


FIG. 16 (color online). Effective probabilities  $P'_{\nu_e \nu_e}$  [(a) and (c)] and  $P'_{\bar{\nu}_e \bar{\nu}_e}$  [(b) and (d)] following adiabatic MSW flavor conversion as functions of  $r$  and  $E$  for both the NH and IH.

The rate of neutrino interaction on a target nucleus  $A$  at radius  $r$  can then be calculated as

$$\lambda_{\nu_{\alpha A}}^{\text{osc}}(r, t) = \frac{R_d^2}{4\pi^2 r^2} \int E^2 \tilde{f}_{\nu_{\alpha}}(t', E, r) \sigma_{\nu_{\alpha A}}(E) dE. \quad (21)$$

In Fig. 17, we show the rate  $\lambda_{\nu_{\alpha A}}^0$  without neutrino oscillations and  $\lambda_{\nu_{\alpha A}}^{\text{osc}}/\lambda_{\nu_{\alpha A}}^0$  for charged-current  $\nu_e$  and  $\bar{\nu}_e$  interactions on  ${}^4\text{He}$  at  $r = 10^5$  km. The cross sections are fitted to the form  $\sigma_{\alpha}[(E - E_0)/\text{MeV}]^n$  by using the spectrally-averaged cross sections listed in Table II of [66]. We find that  $\sigma_{\alpha} = 3.32 \times 10^{-48}$  cm<sup>2</sup>/nucleon,  $E_0 = 19.8$  MeV,  $n = 4.01$  for  $\nu_e + {}^4\text{He} \rightarrow {}^3\text{He} + p + e^-$  and  $\sigma_{\alpha} = 8.19 \times 10^{-48}$  cm<sup>2</sup>/nucleon,  $E_0 = 21.6$  MeV,  $n = 3.76$  for  $\bar{\nu}_e + {}^4\text{He} \rightarrow {}^3\text{H} + n + e^+$ . As collective oscillations are suppressed in our model for the NH, flavor

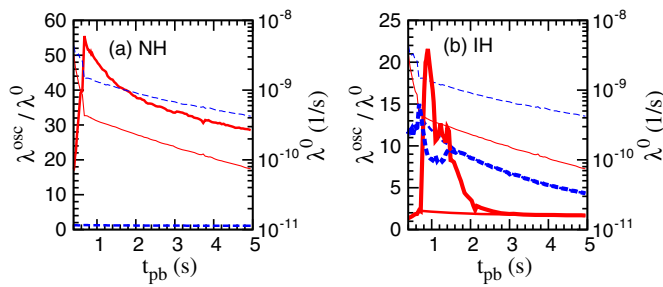


FIG. 17 (color online). (a) The ratio  $\lambda^{\text{osc}}/\lambda^0$  (thick curves) and the rate  $\lambda^0$  without neutrino oscillations (thin curves) for charged-current  $\nu_e$  (red solid curves) and  $\bar{\nu}_e$  (blue dashed curves) interactions on  ${}^4\text{He}$  at  $r = 10^5$  km as functions of  $t_{\text{pb}}$  for the NH. (b) Same as (a) but for the IH. The thickest curves are for the full case including both collective neutrino oscillations and MSW flavor transformation while the thicker curves are for the case of pure MSW flavor transformation.

transformation in this case occurs purely through the MSW effect, which only enhances the  $\nu_e$  interaction rate (see Fig. 16). The time evolution of  $\lambda_{\nu_{\alpha A}}^{\text{osc}}/\lambda_{\nu_{\alpha A}}^0$  basically follows the relative change of the high-energy tail of the  $\nu_e$  and  $\nu_y$  spectra. In the case of IH, there is large enhancement in the  $\nu_e$  interaction rate for  $0.7 \lesssim t_{\text{pb}} \lesssim 2.5$  s and in the  $\bar{\nu}_e$  interaction rate for  $0.7 \lesssim t_{\text{pb}} \lesssim 5$  s. For  $\nu_e$ , the enhancement is due to partial flavor conversion between  $\nu_e$  and  $\nu_y$  through collective oscillations (see Fig. 6). In contrast, the enhancement for  $\bar{\nu}_e$  is mostly due to MSW flavor conversion. In fact, partial flavor conversion through collective oscillations results in a slight reduction of the enhancement in the  $\bar{\nu}_e$  interaction rate for  $0.7 \lesssim t_{\text{pb}} \lesssim 1.5$  s when compared to the case including MSW flavor conversion only.

Neutrino-induced nucleosynthesis in He shells is sensitive to the time integrated rate of (anti)neutrino absorption on  ${}^4\text{He}$ ,  $\Delta n(r) \equiv \int \lambda(r, t) dt$ . We calculate the integral for the first 5 s post bounce and show the enhancement factor  $\Delta n^{\text{osc}}(r)/\Delta n^0(r)$  as a function of radius in Fig. 18. For the He layer located at  $5.5 \times 10^4 \lesssim r \lesssim 4 \times 10^5$  km in our model,  $\Delta n(r)$  for  $\nu_e$  ( $\bar{\nu}_e$ ) absorption on  ${}^4\text{He}$  is enhanced by a factor of  $\sim 32$  ( $\sim 17$ ) for the NH (IH) following adiabatic MSW flavor transformation through the 1–3 resonance. Before this MSW resonance, collective oscillations for the IH result in an enhancement factor of  $\sim 2.2$  and  $\sim 1.5$  for  $\nu_e$  and  $\bar{\nu}_e$  absorption, respectively. Both the collective and MSW flavor transformations will increase the production of  ${}^7\text{Li}$  and  ${}^{11}\text{B}$ . To quantify the increase will require a full calculation of neutrino-induced nucleosynthesis, which is beyond the scope of the present work. The impact of MSW flavor transformation on the production of  ${}^7\text{Li}$  and  ${}^{11}\text{B}$  was explored in [63]. However, this previous study assumed harder neutrino spectra than calculated by our supernova simulations, which makes it difficult to extrapolate their conclusions to our model.

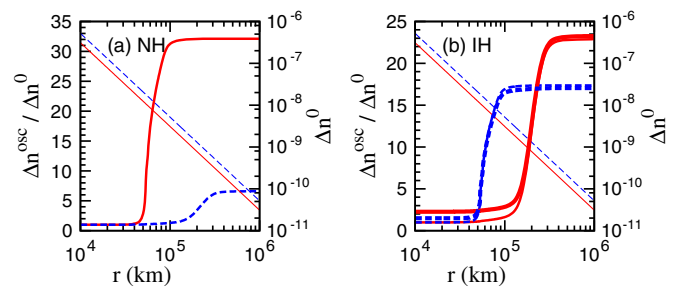


FIG. 18 (color online). (a) The ratio  $\Delta n^{\text{osc}}/\Delta n^0$  (thick curves) and the time-integrated rate  $\Delta n^0$  without neutrino oscillations (thin curves) as functions of  $r$  for charged-current  $\nu_e$  (red solid curves) and  $\bar{\nu}_e$  (blue dashed curves) interactions on  ${}^4\text{He}$  for the NH. (b) Same as (a) but for the IH. The thickest curves are for the full case including both collective neutrino oscillations and MSW flavor transformation while the thicker curves are for the case of pure MSW flavor transformation.

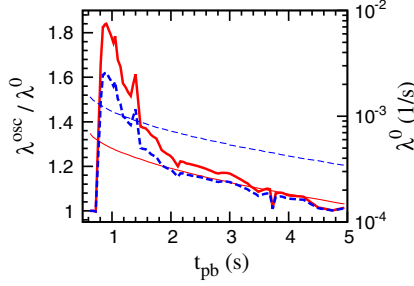


FIG. 19 (color online). The ratios  $\lambda^{\text{osc}}/\lambda^0$  for charged-current interactions of  $\nu_e$  on  $^{138}\text{Ba}$  (red solid curves) and  $^{180}\text{Hf}$  (blue dashed curves) as functions of  $t_{\text{pb}}$  for the IH. The rates  $\lambda^0$  at  $r = 10^4$  km without oscillations (thin curves) are also shown.

### C. Effects on rates of $\nu_e$ absorption by $^{138}\text{Ba}$ and $^{180}\text{Hf}$ and the production of $^{138}\text{La}$ and $^{180}\text{Ta}$

The rare isotopes  $^{138}\text{La}$  and  $^{180}\text{Ta}$  can be produced predominantly by the charged-current interaction of  $\nu_e$  on the preexisting  $^{138}\text{Ba}$  and  $^{180}\text{Hf}$ , respectively. The main production region is in the O/Ne shell of our supernova progenitor and the yields sensitively depend on the neutrino “temperature” [59]. During the first 5 s post bounce,  $n_e(r)$  in the O/Ne shell is much larger than  $n_{e,\text{MSW}}^{13}(E)$  for typical neutrino energies, and the neutrino interaction rates on nuclei can be calculated similarly to Eq. (21) but with  $\tilde{f}_{\nu_\alpha}(t', E, r)$  replaced by  $f_{\nu_\alpha}^{(i)}(t, E)$ . In this case, flavor conversion results from collective oscillations only and the ratio  $\lambda_{\nu_\alpha A}^{\text{osc}}/\lambda_{\nu_\alpha A}^0$  is independent of radius due to cancellation of the  $1/r^2$  dependence for each rate.

We have calculated the rates of reactions (15a) and (15b) with and without neutrino oscillations, using cross sections with power-law dependence on neutrino energy fitted to the spectrally-averaged cross sections adopted in [59]. The enhancement factors  $\lambda_{\nu_\alpha A}^{\text{osc}}/\lambda_{\nu_\alpha A}^0$  for these rates for the IH are shown in Fig. 19. Although collective oscillations enhance the rates of  $\nu_e$  interactions on  $^{138}\text{Ba}$  and  $^{180}\text{Hf}$  by up to  $\sim 80\%$  and  $\sim 60\%$ , respectively, during  $0.8 < t_{\text{pb}} < 5$  s, the time-integrated rates for the first 5 s post bounce are increased by only  $\sim 11.5\%$  and  $\sim 8.5\%$ , respectively. This is because the neutrino luminosity is much higher but collective oscillations are suppressed during the first 0.8 s post bounce. Consequently, while  $\nu_e$  interactions during the cooling phase are substantially enhanced by collective oscillations for the IH, they still contribute subdominantly to the total production of  $^{138}\text{La}$  and  $^{180}\text{Ta}$ .

## VI. EFFECTS OF FLAVOR OSCILLATIONS ON NEUTRINO SIGNALS

For predicting neutrino signals from a Galactic supernova described by our model, the event rate for a particular neutrino interaction with target particles  $i$  in a detector can be approximately calculated as

$$R_i(t) = \frac{N_i R_d^2}{4\pi^2 d^2} \sum_\alpha \int_{E_{\text{th}}}^\infty E^2 f_{\nu_\alpha}^{(f)}(E, t) \sigma_{\nu_\alpha i}(E) dE, \quad (22)$$

where  $N_i$  is the total number of target particles  $i$  in the detector,  $d$  is the distance from the supernova to the Earth, and  $E_{\text{th}}$  is the threshold energy for the interaction. Here we have assumed 100% detection efficiency for simplicity. For the neutrino energy spectra  $f_{\nu_\alpha}^{(f)}$  at the Earth, we neglect the slight modification by the Earth-matter effect [67] and assume  $f_{\nu_\alpha}^{(f)} = \tilde{f}_{\nu_\alpha}(n_e = 0)$ . Specifically, we take

$$f_{\nu_e}^{(f)} = s_{13}^2 f_{\nu_e}^{(i)} + c_{12}^2 c_{13}^2 f_{\nu_x}^{(i)} + s_{12}^2 c_{13}^2 f_{\nu_y}^{(i)}, \quad (23a)$$

$$f_{\nu_x}^{(f)} = s_{12}^2 f_{\nu_x}^{(i)} + c_{12}^2 f_{\nu_y}^{(i)}, \quad (23b)$$

$$f_{\nu_y}^{(f)} = c_{13}^2 f_{\nu_e}^{(i)} + c_{12}^2 s_{13}^2 f_{\nu_x}^{(i)} + s_{12}^2 s_{13}^2 f_{\nu_y}^{(i)}, \quad (23c)$$

$$f_{\bar{\nu}_e}^{(f)} = c_{12}^2 c_{13}^2 f_{\bar{\nu}_e}^{(i)} + s_{12}^2 c_{13}^2 f_{\bar{\nu}_x}^{(i)} + s_{13}^2 f_{\bar{\nu}_y}^{(i)}, \quad (23d)$$

$$f_{\bar{\nu}_x}^{(f)} = s_{12}^2 f_{\bar{\nu}_e}^{(i)} + c_{12}^2 f_{\bar{\nu}_y}^{(i)}, \quad (23e)$$

$$f_{\bar{\nu}_y}^{(f)} = c_{12}^2 s_{13}^2 f_{\bar{\nu}_e}^{(i)} + s_{12}^2 s_{13}^2 f_{\bar{\nu}_x}^{(i)} + c_{13}^2 f_{\bar{\nu}_y}^{(i)}, \quad (23f)$$

for the NH, and

$$f_{\nu_e}^{(f)} = s_{12}^2 c_{13}^2 f_{\nu_e}^{(i)} + c_{12}^2 c_{13}^2 f_{\nu_x}^{(i)} + s_{13}^2 f_{\nu_y}^{(i)}, \quad (24a)$$

$$f_{\nu_x}^{(f)} = c_{12}^2 f_{\nu_e}^{(i)} + s_{12}^2 f_{\nu_y}^{(i)}, \quad (24b)$$

$$f_{\nu_y}^{(f)} = s_{12}^2 s_{13}^2 f_{\nu_e}^{(i)} + c_{12}^2 s_{13}^2 f_{\nu_x}^{(i)} + c_{13}^2 f_{\nu_y}^{(i)}, \quad (24c)$$

$$f_{\bar{\nu}_e}^{(f)} = s_{13}^2 f_{\bar{\nu}_e}^{(i)} + s_{12}^2 c_{13}^2 f_{\bar{\nu}_x}^{(i)} + c_{12}^2 c_{13}^2 f_{\bar{\nu}_y}^{(i)}, \quad (24d)$$

$$f_{\bar{\nu}_x}^{(f)} = c_{12}^2 f_{\bar{\nu}_e}^{(i)} + s_{12}^2 f_{\bar{\nu}_y}^{(i)}, \quad (24e)$$

$$f_{\bar{\nu}_y}^{(f)} = c_{13}^2 f_{\bar{\nu}_e}^{(i)} + s_{12}^2 s_{13}^2 f_{\bar{\nu}_x}^{(i)} + c_{12}^2 s_{13}^2 f_{\bar{\nu}_y}^{(i)}, \quad (24f)$$

for the IH. In the above equations,  $c_{ij}$  and  $s_{ij}$  stand for  $\cos \theta_{ij}$  and  $\sin \theta_{ij}$ , respectively.

We have calculated the expected neutrino signals in a 34 kton liquid argon time projection chamber (LArTPC) detector and the Super-Kamiokande (Super-K) detector for a Galactic supernova at  $d = 10$  kpc. The included interaction channels are

$$\nu_e + {}^{40}\text{Ar} \rightarrow e^- + {}^{40}\text{K}^*, \quad (25a)$$

$$\bar{\nu}_e + {}^{40}\text{Ar} \rightarrow e^+ + {}^{40}\text{Cl}^*, \quad (25b)$$

$$\nu_\alpha + e^- \rightarrow \nu_\alpha + e^-, \quad (25c)$$

for the LArTPC detector, and

$$\bar{\nu}_e + p \rightarrow e^+ + n, \quad (26a)$$

$$\nu_\alpha + e^- \rightarrow \nu_\alpha + e^-, \quad (26b)$$

$$\nu_\alpha + {}^{16}\text{O} \rightarrow \nu_\alpha + {}^{16}\text{O}, \quad (26c)$$

$$\nu_e + {}^{16}\text{O} \rightarrow e^- + {}^{16}\text{F}^*, \quad (26d)$$

$$\bar{\nu}_e + {}^{16}\text{O} \rightarrow e^+ + {}^{16}\text{N}^*, \quad (26e)$$

for the Super-K detector. The cross sections for neutrino interactions on  ${}^{16}\text{O}$  and  ${}^{40}\text{Ar}$  have been computed in [68]. The numerical values for all cross sections are taken from the data compiled in [9]. In Fig. 20, we show the number of all neutrino events in time bins of 5, 20, and 200 ms for the neutronization burst, the accretion phase, and the proto-neutron star cooling phase, respectively, as a function of time.

The neutronization burst could be readily seen in the LArTPC detector if there were no neutrino oscillations. However, the burst completely disappears for the NH. For the IH, there might still be a chance to identify the burst from the dominant interaction channel of  $\nu_e$  capture on  ${}^{40}\text{Ar}$ . This can be understood by examining Eqs. (23) and (24). With  $c_{12}^2 c_{13}^2 \sim 0.69$ ,  $s_{12}^2 c_{13}^2 \sim 0.31$ , and  $s_{13}^2 \sim 0$ , we have  $f_{\nu_e}^{(f)} \sim f_{\nu_{\mu(\tau)}}$  for the NH and  $f_{\nu_e}^{(f)} \sim 0.31 f_{\nu_e} + 0.69 f_{\nu_{\mu(\tau)}}$  for the IH when there are no collective neutrino oscillations. As the  $\nu_{\mu(\tau)}$  flux is much smaller compared to  $\nu_e$  during the neutronization burst, the number of events with oscillations is strongly limited. For the Super-K detector, the dominant detection channel is  $\bar{\nu}_e$  absorption on protons and the  $\bar{\nu}_e$  flux at the detector is  $f_{\bar{\nu}_e}^{(f)} \sim 0.69 f_{\bar{\nu}_e} + 0.31 f_{\bar{\nu}_{\mu(\tau)}}$  for the NH and  $f_{\bar{\nu}_e}^{(f)} \sim f_{\bar{\nu}_{\mu(\tau)}}$  for the IH. Thus, there will be more events for the IH because  $\bar{\nu}_{\mu(\tau)}$  have a higher average energy than  $\bar{\nu}_e$ . Note that if the distance to the supernova is much closer than 10 kpc, there will be many more events during the neutronization burst so that the rising time of the  $\bar{\nu}_e$  signal may be used to distinguish the neutrino mass hierarchy [69].

During the accretion phase, the time profiles of the events in the two detectors behave quite differently for either mass hierarchy. For the NH, the  $\bar{\nu}_e$  luminosity plateau at emission (see Fig. 2) can still be observed in the Super-K detector, but in the LArTPC detector, the event rate basically follows the decreasing  $\nu_{\mu(\tau)}$  luminosity at emission. For the IH, both detectors will see a decreasing number of events per bin with time, but the rate of decrease will be larger for the Super-K detector. If the time profiles of (anti-)neutrino luminosities at emission in our model are generic for supernovae, it will be possible to utilize the time profiles of the events in the two detectors, e.g., by forming a

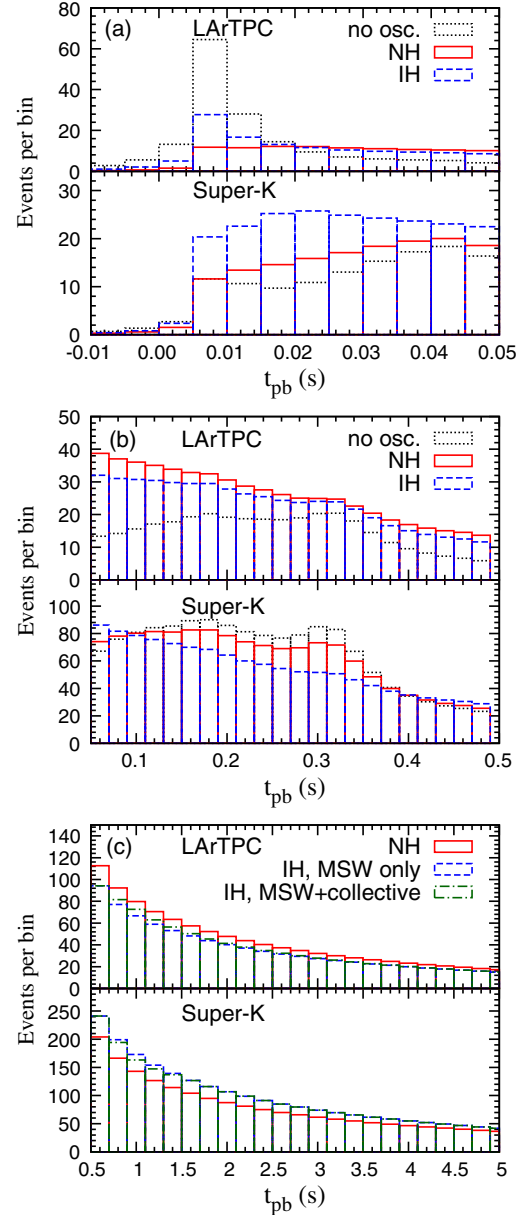


FIG. 20 (color online). The number of all neutrino events per time bin as a function of time for an LArTPC detector and the Super-K detector, respectively, during (a) the neutronization burst, (b) the accretion phase, and (c) the proto-neutron star cooling phase of a Galactic supernova at a distance of 10 kpc.

ratio of the respective number of events per time bin, to infer the neutrino mass hierarchy.

During the cooling phase, the time profiles of the events are rather similar for both mass hierarchies and whether collective oscillations are included or not. As the 1-2 mixing is entirely suppressed in the region of collective oscillations, it is straightforward to show from Eqs. (23) and (24) that the neutrino signals will always be between the cases of pure adiabatic MSW flavor transformation for the NH and IH. The similarity of the event time profiles in different scenarios of neutrino oscillations is further



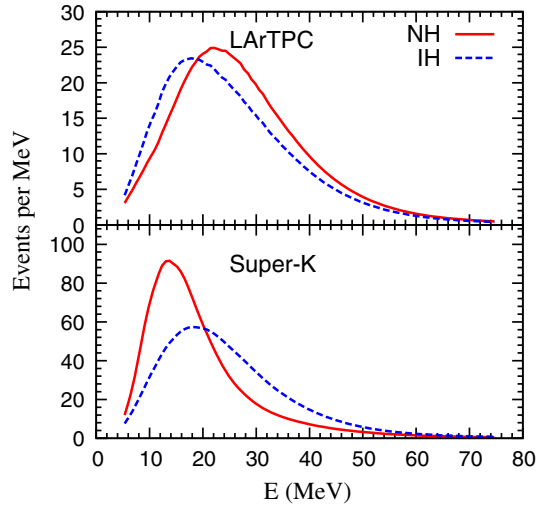


FIG. 21 (color online). Time-integrated energy spectra of neutrino events during the first 0.5 s for the LArTPC and Super-K detectors.

enhanced by the convergence of all neutrino spectra during the cooling phase.

From the above discussion, it is clear that the neutrino signals during the accretion phase give a better chance to resolve the neutrino mass hierarchy. During this phase, there are substantial differences in the (anti)neutrino spectra between the electron and  $\mu(\tau)$  flavors and the total number of expected events is also relatively large compared to the neutronization burst. It is thus interesting to examine the energy spectra of the neutrino events during the accretion phase for both mass hierarchies. In Fig. 21, we show the time-integrated neutrino spectra during the first 0.5 s for the LArTPC and Super-K detectors, assuming that the neutrino energy can be inferred from detection. It can be seen that for the NH, the spectrum in the Super-K detector has a much lower average energy and smaller spread compared with the spectrum in the same detector for the IH or the spectrum in the LArTPC detector for either mass hierarchy. Thus, assuming that collective neutrino oscillations are indeed strongly suppressed during the accretion phase of supernova explosion, we expect that the NH can be clearly identified if a large difference in the neutrino spectra is detected between the Super-K and LArTPC detectors. This identification can be made more robust by using the different time profiles for the two detectors in addition.

## VII. CONCLUSIONS

We have shown that in order to understand the effects of neutrino flavor oscillations on supernova nucleosynthesis and on the neutrino signals, a detailed calculation including both collective oscillations and the subsequent MSW flavor transformation has to be carried out to derive the flavor conversion probabilities as functions of the emission time, energy, propagation angle, and arrival radius for a neutrino.

We have explicitly described a detailed scheme of calculation and implemented it by employing the time-dependent neutrino spectra and electron density profiles from a spherically symmetric supernova model with an  $18M_{\odot}$  progenitor. We find that collective neutrino oscillations are not only sensitive to the detailed neutrino energy and angular distributions at emission, but also to the time evolution of these distributions and the electron density profile due to the nonlinear nature of the flavor evolution equation as discussed in Sec. IV.

We have shown that in our supernova model, collective neutrino oscillations happen only for the IH, mostly in the neutrino sector during the first 5 s of the proto-neutron star cooling phase, due to the dominant emission of  $\bar{\nu}_{\mu(\tau)}$  over  $\bar{\nu}_e$ . The radius/temperature at which these oscillations occur is in general too far/low to have a direct impact on  $Y_e$  before free nucleons are assembled into  $\alpha$  particles. In addition, there is no effect on the rate of  $\bar{\nu}_e$  capture on protons for the temperature range of  $1 \lesssim T \lesssim 3$  GK, which is relevant for the  $\nu p$  process in the neutrino-driven wind. Thus, the outcome of this process in our supernova model is not affected by collective neutrino oscillations as discussed in Sec. VA. However, collective oscillations may still enhance somewhat the production of the rare isotopes  $^{138}\text{La}$  and  $^{180}\text{Ta}$  as shown in Sec. VC. We have also calculated the MSW flavor transformation that happens in the C/O and He shells of the supernova for the first 5 s of post-bounce time, in order to evaluate the impact of neutrino oscillations on the neutrino-induced nucleosynthesis in the He shell and on the neutrino signals. We find that the charged-current interaction rates of  $\nu_e$  ( $\bar{\nu}_e$ ) on  $^4\text{He}$  are greatly enhanced by the MSW flavor transformation for the NH (IH). This may impact the production of  $^7\text{Li}$  and  $^{11}\text{B}$  as studied in [63].

For the neutrino signals from our supernova model, we have calculated the number of events per time bin for different neutrino emission phases for the Super-Kamiokande detector and a hypothetical 34 kton liquid argon detector. The results suggest that for a Galactic supernova of this kind, the events from the neutronization burst may not be enough to identify the burst. However, it may be possible to use the time profiles of events during the accretion phase and the associated neutrino spectra in these two detectors to infer the yet unknown neutrino mass hierarchy. For the cooling phase, we have shown that the effects of collective oscillations are in general small, limited by the difference between the cases of pure MSW flavor transformation for the NH and IH.

Although our results seem to suggest that collective neutrino oscillations do not have a large impact on either the nucleosynthesis or the neutrino signals, cautions must be mentioned as there are a number of issues in modeling such oscillations in supernovae. First, in our treatment here, we have assumed azimuthal symmetry around the radial direction for collective oscillations. The effect of relaxing this symmetry [28] needs to be further examined and may

require a full six-dimensional calculation for neutrinos emitted in different parts of the proto-neutron star surface. Second, it has been suggested recently that the coherence between different neutrino mass eigenstates may not be maintained by the time collective oscillations occur, due to the very small wave-packet size of neutrinos at production [35]. Detailed examination of this effect in connection with the processes of neutrino production is thus required. Third, although studies of flavor instabilities suggest that the contribution to the effective Hamiltonian from those neutrinos scattered by nuclei outside a proto-neutron star, the so-called neutrino “halo,” may further suppress collective oscillations during the accretion phase [24,26], this remains to be confirmed by a self-consistent calculation. Fourth, our view of collective oscillations in particular and neutrino flavor transformation in general might be changed by the apparently subdominant beyond-the-mean-field contribution [27], the neutrino spin coherence [36], and the neutrino magnetic moment [70]. Last but not the least, as we have demonstrated in this paper, the outcome of neutrino flavor oscillations is sensitive to the input from the supernova model. For example, any change in neutrino spectra from supernova models with improved treatment of neutrino interaction with matter in the decoupling region [71,72] will require reexamination of the problem of supernova neutrino oscillations.

In summary, this work represents a small step towards the understanding of supernova neutrino oscillations and their impact. In view of the importance of supernova

nucleosynthesis to the production history of various nuclei in our universe, along with the high reward of utilizing neutrino signals from a future Galactic supernova to learn about supernova physics and neutrino properties, further studies that take into account all the issues mentioned above, not for one, but for a large number of models with different progenitors, must be carried out in order to fully understand the effects of neutrino oscillations in supernovae and the associated rich physics.

## ACKNOWLEDGMENTS

M.-R. W. is partly supported by the Alexander von Humboldt Foundation. Y.-Z. Q. is partly supported by the United States Department of Energy (DE-FG02-87ER40328). L. H. and G. M. P. are partly supported by the Deutsche Forschungsgemeinschaft through Contract No. SFB 634, the Helmholtz International Center for FAIR within the framework of the LOEWE program launched by the state of Hesse and the Helmholtz Association through the Nuclear Astrophysics Virtual Institute (VH-VI-417). T. F. acknowledges support from the Narodowe Centrum Nauki (NCN) within the “Sonata” program under Contract No. UMO-2013/11/D/ST2/02645. M.-R. W. and G. M. P. gratefully thank Andre Sieverding for helpful discussions. This work was carried out, in part, using computing resources at the University of Minnesota Supercomputing Institute.

- 
- [1] H. A. Bethe and J. R. Wilson, *Astrophys. J.* **295**, 14 (1985).
  - [2] H.-T. Janka, *Annu. Rev. Nucl. Part. Sci.* **62**, 407 (2012).
  - [3] Y.-Z. Qian and S. E. Woosley, *Astrophys. J.* **471**, 331 (1996).
  - [4] A. Arcones and F.-K. Thielemann, *J. Phys. G* **40**, 013201 (2013).
  - [5] R. I. Epstein, S. A. Colgate, and W. C. Haxton, *Phys. Rev. Lett.* **61**, 2038 (1988).
  - [6] S. E. Woosley, D. H. Hartmann, R. D. Hoffman, and W. C. Haxton, *Astrophys. J.* **356**, 272 (1990).
  - [7] P. Banerjee, W. Haxton, and Y.-Z. Qian, *Phys. Rev. Lett.* **106**, 201104 (2011).
  - [8] P. Banerjee, Y.-Z. Qian, W. C. Haxton, and A. Heger, *Phys. Rev. Lett.* **110**, 141101 (2013).
  - [9] K. Scholberg, *Annu. Rev. Nucl. Part. Sci.* **62**, 81 (2012).
  - [10] K. A. Olive *et al.* (Particle Data Group), *Chin. Phys. C* **38**, 090001 (2014).
  - [11] L. Wolfenstein, *Phys. Rev. D* **17**, 2369 (1978).
  - [12] S. P. Mikheyev and A. Y. Smirnov, *Yad. Fiz.* **42**, 1441 (1985).
  - [13] H. Duan, G. M. Fuller, and Y.-Z. Qian, *Annu. Rev. Nucl. Part. Sci.* **60**, 569 (2010).
  - [14] G. G. Raffelt, *Phys. Rev. D* **83**, 105022 (2011).
  - [15] H. Duan and A. Friedland, *Phys. Rev. Lett.* **106**, 091101 (2011).
  - [16] S. Chakraborty, T. Fischer, A. Mirizzi, N. Saviano, and R. Tomas, *Phys. Rev. Lett.* **107**, 151101 (2011).
  - [17] S. Chakraborty, T. Fischer, A. Mirizzi, N. Saviano, and R. Tomas, *Phys. Rev. D* **84**, 025002 (2011).
  - [18] S. Galais and C. Volpe, *Phys. Rev. D* **84**, 085005 (2011).
  - [19] M.-R. Wu and Y.-Z. Qian, *Phys. Rev. D* **84**, 045009 (2011).
  - [20] A. Mirizzi and P. D. Serpico, *Phys. Rev. Lett.* **108**, 231102 (2012).
  - [21] Y. Pehlivan, A. Balantekin, T. Kajino, and T. Yoshida, *Phys. Rev. D* **84**, 065008 (2011).
  - [22] A. Banerjee, A. Dighe, and G. Raffelt, *Phys. Rev. D* **84**, 053013 (2011).
  - [23] S. Sarikas, G. G. Raffelt, L. Hudepohl, and H.-T. Janka, *Phys. Rev. Lett.* **108**, 061101 (2012).
  - [24] S. Sarikas, I. Tamborra, G. Raffelt, L. Hudepohl, and H.-T. Janka, *Phys. Rev. D* **85**, 113007 (2012).
  - [25] N. Saviano, S. Chakraborty, T. Fischer, and A. Mirizzi, *Phys. Rev. D* **85**, 113002 (2012).

- [26] J. F. Cherry, J. Carlson, A. Friedland, G. M. Fuller, and A. Vlasenko, *Phys. Rev. Lett.* **108**, 261104 (2012).
- [27] C. Volpe, D. Väänänen, and C. Espinoza, *Phys. Rev. D* **87**, 113010 (2013).
- [28] G. Raffelt, S. Sarikas, and D. de Sousa Seixas, *Phys. Rev. Lett.* **111**, 091101 (2013).
- [29] G. Raffelt and D. de S. Seixas, *Phys. Rev. D* **88**, 045031 (2013).
- [30] J. F. Cherry, J. Carlson, A. Friedland, G. M. Fuller, and A. Vlasenko, *Phys. Rev. D* **87**, 085037 (2013).
- [31] A. Vlasenko, G. M. Fuller, and V. Cirigliano, *Phys. Rev. D* **89**, 105004 (2014).
- [32] A. Mirizzi, *Phys. Rev. D* **88**, 073004 (2013).
- [33] H. Duan, *Phys. Rev. D* **88**, 125008 (2013).
- [34] S. Chakraborty, A. Mirizzi, N. Saviano, and D. de S. Seixas, *Phys. Rev. D* **89**, 093001 (2014).
- [35] E. Akhmedov, J. Kopp, and M. Lindner, [arXiv:1405.7275](https://arxiv.org/abs/1405.7275).
- [36] A. Vlasenko, G. M. Fuller, and V. Cirigliano, [arXiv:1406.6724](https://arxiv.org/abs/1406.6724).
- [37] T. Fischer, S. Whitehouse, A. Mezzacappa, F.-K. Thielemann, and M. Liebendorfer, *Astron. Astrophys.* **517**, A80 (2010).
- [38] M. Kachelriess, R. Tomas, R. Buras, H.-T. Janka, A. Marek *et al.*, *Phys. Rev. D* **71**, 063003 (2005).
- [39] C. Fröhlich, G. Martínez-Pinedo, M. Liebendorfer, F.-K. Thielemann, E. Bravo, W. R. Hix, K. Langanke, and N. T. Zinner, *Phys. Rev. Lett.* **96**, 142502 (2006).
- [40] J. Pruet, R. Hoffman, S. Woosley, H.-T. Janka, and R. Buras, *Astrophys. J.* **644**, 1028 (2006).
- [41] L. Huther, T. Fischer, G. Martínez-Pinedo, and K. Langanke, *Proc. Sci.*, NICXII2012 (2012) 120.
- [42] K. Nakamura *et al.* (Particle Data Group), *J. Phys. G* **37**, 075021 (2010).
- [43] F. An *et al.* (DAYA-BAY Collaboration), *Phys. Rev. Lett.* **108**, 171803 (2012).
- [44] H. Duan, G. M. Fuller, J. Carlson, and Y.-Z. Qian, *Phys. Rev. D* **74**, 105014 (2006).
- [45] B. Dasgupta and A. Dighe, *Phys. Rev. D* **77**, 113002 (2008).
- [46] J. Gava and C. Volpe, *Phys. Rev. D* **78**, 083007 (2008).
- [47] G. M. Fuller, R. W. Mayle, J. R. Wilson, and D. N. Schramm, *Astrophys. J.* **322**, 795 (1987).
- [48] G. Sigl and G. Raffelt, *Nucl. Phys.* **B406**, 423 (1993).
- [49] J. T. Pantaleone, *Phys. Rev. D* **46**, 510 (1992).
- [50] A. Esteban-Pretel, A. Mirizzi, S. Pastor, R. Tomàs, G. G. Raffelt, P. D. Serpico, and G. Sigl, *Phys. Rev. D* **78**, 085012 (2008).
- [51] G. L. Fogli, E. Lisi, A. Marrone, and A. Mirizzi, *J. Cosmol. Astropart. Phys.* **12** (2007) 010.
- [52] J. F. Cherry, G. M. Fuller, J. Carlson, H. Duan, and Y.-Z. Qian, *Phys. Rev. D* **82**, 085025 (2010).
- [53] J. F. Cherry, M.-R. Wu, J. Carlson, H. Duan, G. M. Fuller, and Y.-Z. Qian, *Phys. Rev. D* **84**, 105034 (2011).
- [54] J. F. Cherry, M.-R. Wu, J. Carlson, H. Duan, G. M. Fuller, and Y.-Z. Qian, *Phys. Rev. D* **85**, 125010 (2012).
- [55] B. Dasgupta, A. Dighe, G. G. Raffelt, and A. Y. Smirnov, *Phys. Rev. Lett.* **103**, 051105 (2009).
- [56] A. Mirizzi and R. Tomas, *Phys. Rev. D* **84**, 033013 (2011).
- [57] A. Friedland, *Phys. Rev. Lett.* **104**, 191102 (2010).
- [58] B. Dasgupta, A. Mirizzi, I. Tamborra, and R. Tomas, *Phys. Rev. D* **81**, 093008 (2010).
- [59] A. Heger, E. Kolbe, W. C. Haxton, K. Langanke, G. Martínez-Pinedo, and S. E. Woosley, *Phys. Lett. B* **606**, 258 (2005).
- [60] A. Byelikov, T. Adachi, H. Fujita, K. Fujita, Y. Fujita, K. Hatanaka, A. Heger, Y. Kalmykov, K. Kawase, K. Langanke, G. Martínez-Pinedo, K. Nakanishi, P. von Neumann-Cosel, R. Neveling, A. Richter, N. Sakamoto, Y. Sakemi, A. Shevchenko, Y. Shimbara, Y. Shimizu, F. D. Smit, Y. T ameshige, A. Tamii, S. E. Woosley, and M. Yosoi, *Phys. Rev. Lett.* **98**, 082501 (2007).
- [61] G. Martínez-Pinedo, B. Ziebarth, T. Fischer, and K. Langanke, *Eur. Phys. J. A* **47**, 98 (2011).
- [62] H. Duan, A. Friedland, G. C. McLaughlin, and R. Surman, *J. Phys. G* **38**, 035201 (2011).
- [63] T. Yoshida, T. Kajino, H. Yokomakura, K. Kimura, A. Takamura, and D. H. Hartmann, *Astrophys. J.* **649**, 319 (2006).
- [64] C. Horowitz and G. Li, *Phys. Rev. Lett.* **82**, 5198 (1999).
- [65] S. Woosley, A. Heger, and T. Weaver, *Rev. Mod. Phys.* **74**, 1015 (2002).
- [66] D. Gazit and N. Barnea, *Phys. Rev. Lett.* **98**, 192501 (2007).
- [67] E. Borriello, S. Chakraborty, A. Mirizzi, P. D. Serpico, and I. Tamborra, *Phys. Rev. D* **86**, 083004 (2012).
- [68] E. Kolbe, K. Langanke, G. Martínez-Pinedo, and P. Vogel, *J. Phys. G* **29**, 2569 (2003).
- [69] P. D. Serpico, S. Chakraborty, T. Fischer, L. Hudepohl, H.-T. Janka, and A. Mirizzi, *Phys. Rev. D* **85**, 085031 (2012).
- [70] A. de Gouvea and S. Shalgar, *J. Cosmol. Astropart. Phys.* **04** (2013) 018.
- [71] G. Martínez-Pinedo, T. Fischer, A. Lohs, and L. Huther, *Phys. Rev. Lett.* **109**, 251104 (2012).
- [72] L. Roberts, S. Reddy, and G. Shen, *Phys. Rev. C* **86**, 065803 (2012).